

Effect of Low Temperature on Fatigue Crack Formation and Microstructure-Scale Growth from Corrosion Damage in Al-Zn-Mg-Cu

JAMES T. BURNS and RICHARD P. GANGLOFF

The strong effect of cold temperature on the fatigue resistance of 7075-T651 is established. As temperature decreases from 296 K to 183 K (23 °C to -90 °C), the formation life for cracking about pit and EXCO corrosion perimeters increases, microstructure scale crack growth rates decrease in the range from 20 to 500 μm beyond the corrosion topography, and long crack growth rates similarly decline. Fatigue crack surface features correlate with reduced hydrogen embrittlement with decreasing temperature fed by localized H produced during precorrosion for pit and EXCO-proximate cracks, as well as by crack tip H produced by water vapor reaction during stressing for all crack sizes. The importance of the former H source increases with decreasing temperature for cracks sized below 200 μm . Decreasing temperature to 223 K (-50 °C) eliminates the contribution of environmental H through interaction of reduced water vapor pressure in equilibrium with ice and reduced H diffusion. The Knudsen flow model and exposure parameter, $P_{\text{H}_2\text{O}}/f$, enables improved modeling of temperature dependent crack propagation, but does not fully describe low temperature fatigue behavior due to possible rate limitation by H diffusion. Further decreases in MSC da/dN to 183 K (-90 °C) are related to reduced mobility of the corrosion-precharged H which may associate with vacancies from dissolution. Crack formation, and growth rates correlate with either elastic stress intensity range or cyclic crack tip opening displacement, and are available to predict corrosion effects on airframe fatigue for the important low temperature regime.

DOI: 10.1007/s11661-012-1374-3

© The Minerals, Metals & Materials Society and ASM International 2012

I. INTRODUCTION

PROGNOSIS of component fatigue performance (initiation and microstructurally small crack growth) at progressively smaller size scales requires a predictive model of cracking informed by understanding of the interaction of loading, crack-formation feature, local microstructure, and environment.^[1] Failure analyses^[2-4] suggest that the interaction of ground-based corrosion with fatigue in flight is of particular importance to airframe prognosis.^[5-7] Micro-mechanical and continuum models of fatigue life in Al alloys have been put forth for cracks emanating from microstructural constituents ($\sim 25 \mu\text{m}$)^[1,8-10] or localized corrosion topography (~ 250 to $1,000 \mu\text{m}$).^[11-22] Recent work established the foundation for such modeling including formation feature morphology, relevance of linear elastic fracture mechanics (LEFM), fatigue crack formation life (N_i), and microstructure-scale crack (MSC) propagation rates

(da/dN).^[11,12,23,24] This prior research focused on fatigue of an Al-Zn-Mg-Cu alloy in ambient temperature moist air. However, flight environments range from salt spray at near sea-level to low water vapor pressures and cold temperatures at higher altitudes.^[25-27] Applying fracture mechanics models with ambient temperature-moist air fatigue properties to cracking in cold environments leads to highly conservative life predictions.^[28,29] As such a better empirical and mechanistic understanding of low temperature fatigue is needed.

Extensive experiments and theory establish that the deleterious effect of moist environment on fatigue in Al alloys is due to hydrogen embrittlement following crack tip production and uptake of atomic hydrogen (H) from either chemical reaction of water molecules on aluminum, or coupled anodic and cathodic electrochemical processes at the crack tip.^[30-32] A large body of work debated the atomistic mechanisms of H-enhanced fatigue.^[30,33-41] For precipitation hardened Al stressed in an ambient temperature humid environment, H-enhanced fatigue propagation in the mid to low Paris regime results in facet-like features on the crack surface which are parallel to $\{100\}$, $\{110\}$ and high index $\{hkl\}$ planes.^[33,42,43] Gupta and Agnew reported similar features, with identical crystallographic characteristics, on a fatigue crack surface emerging from constituent particle clusters in 7075-T651 stressed in moist air at 296 K and 223 K (23 °C and -50 °C).^[44] Such features are not produced by fatigue in ultra-high vacuum, which often

JAMES T. BURNS, formerly Air Force Research Laboratory Materials and Manufacturing Directorate (AFRL/RX), Wright Patterson Air Force Base, OH 45433, is now Research Assistant Professor with the Department of Materials Science and Engineering, University of Virginia, Charlottesville, VA 22904. Contact e-mail: jtb5r@virginia.edu RICHARD P. GANGLOFF, Professor, is with the Department of Materials Science and Engineering, University of Virginia.

Manuscript submitted November 28, 2011.

Article published online September 29, 2012

involves {111} facets and slip band cracking (SBC) for Al alloys prone to planar slip.^[45] These precise crystallographic measurements, combined with TEM observations of crack wake dislocation substructure formed by dynamic recovery during fatigue,^[46,47] were speculatively interpreted to support cracking by hydrogen enhanced decohesion (HEDE).^[35,36] From this H cracking basis, extensive research established mass transport and reaction based models that quantitatively predict the dependence of fatigue crack growth (FCG) rate as a function of the ratio of water vapor pressure to frequency ($P_{\text{H}_2\text{O}}/f$).^[32,48-51] The role of crack tip H diffusion in altering the da/dN vs $P_{\text{H}_2\text{O}}/f$ relationship was also considered.^[30,34] These environmental exposure and diffusion descriptions augment the important dependence of da/dN on stress intensity range ($\Delta K = K_{\text{max}} - K_{\text{min}}$) and K_{max} . The crack tip embrittlement mechanism and aspects of the mass transport, reaction, and diffusion sequence that delivers environmental H are sensitive to lowered temperature and water vapor pressure. As such, this hydrogen embrittlement scenario provides a framework to understand the temperature dependence of airframe fatigue.

Uncertainties exist which hinder airframe prognosis. First, crack formation and microstructure scale propagation were characterized for pristine-surface- and corrosion-to-fatigue transitions at 296 K (23 °C) in moist air or nitrogen^[23,52]; however, quantitative studies have not been established as a function of temperature below ambient. Second, MSC growth rates are not available for fatigue at cold temperatures to either test models of unique growth behavior or enable prognosis.^[1,53-57] Third, two sources of H are relevant to fatigue from localized corrosion sites; H dissolved in the alloy proximate to and during corrosion, as well as H produced at a forming/growing crack tip. The relative impact of precorrosion-produced H vs crack tip reaction H has not been established as a function of temperature. Finally, the hypothesis that fatigue crack growth kinetics are dominated by the water vapor pressure present at a given flight altitude and low temperature has not been tested in the framework of $P_{\text{H}_2\text{O}}/f$ modeling.^[32,33,48-51] Confirming this hypothesis would enable a temperature dependent FCG modeling methodology within current fatigue life prediction codes (such as AFGROW^[58]), with the material property input model given as da/dN as a function of ΔK , K_{max} , and $P_{\text{H}_2\text{O}}/f$.

The objectives of this work are three-fold. First, quantitatively characterize the effect of temperature on fatigue crack formation life and microstructure-scale crack propagation kinetics associated with precorrosion in a high-strength aerospace Al alloy. Second, test the hypothesis that water vapor pressure controls the rate of FCG for a range of low temperatures. Third, develop an understanding of low-temperature crack formation and propagation mechanisms; specifically the relative influence of H produced by precorrosion vs H evolved during cyclic plastic deformation.

II. EXPERIMENTAL METHODS

A 50.8 mm thick, rolled 7075-T651 plate (Al-5.7Zn-2.53Mg-1.66Cu-0.263Fe-0.06Si-0.026Mn-0.19Cr-0.02Ti;

wt pct) from the DARPA Structural Integrity Prognosis System program was investigated.^[1,59] The average grain size ranges were 1 to 2 mm, 50 to 74 μm and 8 to 19 μm , in the longitudinal (L), transverse (T) and short-transverse (S) directions, respectively, with a partially recrystallized microstructure.^[1] The monotonic tensile yield strength (σ_{YS}) was 508 MPa (L -oriented), ultimate tensile strength (σ_{UTS}) was 598 MPa, and plane strain fracture toughness was 33 MPa $\sqrt{\text{m}}$ (L - T).^[59] Fatigue experiments were performed on rectangular gauge specimens machined so that the thickness (parallel to the S direction) was centered 7.0 mm from the plate surface, with the tensile axis parallel to L . Gauge length was 30.5 mm, thickness was 7.6 mm and width was 19.1 mm.

Prior to fatigue, isolated-controlled pitting and EXCO-solution exposures were used to produce localized corrosion damage. Individual pits were formed galvanostatically with a constant current of 1.5 mA/pit and a solution of 0.1 M AlCl_3 + 0.86 M NaCl + HCl added to lower the pH to 2. This protocol was applied to both L - S surfaces of the fatigue specimen, at the mid-length position along L , to produce a total of six semi-ellipsoidal pits; each ~ 230 μm deep (T_p in the T direction), ~ 630 μm in surface length (S_p) along S , and ~ 630 μm height (L_p) along L . Details of the corrosion protocol and specimen are reported elsewhere.^[23,52] Additionally, one L - S surface per specimen (no corner exposure) was exposed to EXCO solution for 3 hours in accordance with ASTM G-34.^[60] After corrosion, all specimens were rinsed and ultrasonically cleaned for 15 minutes in methanol, dried with nitrogen, then stored at ambient temperature in a desiccator with anhydrous calcium sulfate.

Constant amplitude uniaxial fatigue testing was performed on precorroded specimens in accordance with ASTM E466.^[61] A micrometer was used to center the specimen in a hydraulically actuated grip equipped with 90 deg diamond serrated wedges and load train alignment was validated according to ASMT E1012.^[62] For baseline loading, maximum applied-uniform tensile stress (σ_{max}) was 200 MPa, stress ratio ($R = \sigma_{\text{min}}/\sigma_{\text{max}}$) was 0.5, and frequency was 30 Hz. Tests were performed at room temperature [~ 296 K (~ 23 °C)] in water vapor saturated nitrogen (RH >85 pct), and in dry nitrogen (99.99 pct pure) at 223 K and 183 K (-50 °C and -90 °C). Each environment was maintained in a plexi-glass chamber O-ring sealed to the specimen, the seal was not airtight resulting in moisture ingress during fatigue testing. The values of the exposure parameter ($P_{\text{H}_2\text{O}}/f$) for testing at 296 K, 223 K, and 183 K (23 °C, -50 °C, and -90 °C) were 80, 0.133, and 0.0003 Pa s, respectively. These calculations assume that the residual-contaminant water vapor in N_2 concentrates as ice on the specimen surface, with the resulting vapor pressure ($P_{\text{H}_2\text{O-ICE}}$) given by the gas equilibrium above solid ice at the given temperature.^[1,63] Moisture entry to the cell during testing did not change these exposure levels and, as such, was not important.

In order to quantitatively measure fatigue crack formation and propagation behavior, a programmed loading sequence was periodically interspersed to create marks on the fracture surface, consistent with prior

work.^[23,52] For corroded specimens, marker-band loads were applied at $\sigma_{\max} = 200$ MPa, $R = 0.1$ and $f = 10$ Hz. For the 296 K (23 °C) environment, the loading sequence consisted of an initial 5,000 baseline cycles, followed by the repeating sequence of 5 times (25 marker cycles + 50 baseline cycles) + 10,000 baseline cycles. For 223 K (−50 °C) the sequence was: 10,000 initial baseline cycles followed by the repeating sequence of 5 times (250 marker cycles + 400 baseline cycles) + 385,000 baseline cycles. For 183 K (−90 °C) the sequence was: 10,000 initial baseline cycles followed by the repeating sequence of 5 times (500 marker cycles + 1,000 baseline cycles) + 690,000 baseline cycles. All 296 K (23 °C)-humid specimens failed during marker-band cycling. For the 223 K and 183 K (−50 °C and −90 °C) N₂ specimens, once the desired number of marker-band sequences was applied (generally ≈ 15), the environment was removed and specimen was fatigued to failure at $\sigma_{\max} = 400$ MPa and $R = 0.1$ during warming to ambient. This loading and environment change produced a distinct fracture surface morphology that allowed low temperature fatigue crack growth to be discerned.

Fatigue crack growth rate tests were guided by ASTM E647^[64] using *L-T* oriented compact tension (*C-T*) specimens with a height (*H*) of 61 mm, width (*W*) of 64 mm, thickness (*B*) of 6.4 mm, and notch depth of 1.5 mm. Specimen thickness was centered 7.0 mm from the plate surface. Variable temperature tests were performed in water saturated N₂ at 296 K (23 °C) or in dry N₂ (99.99 pct purity) at 221 K (−52 °C) ($P_{\text{H}_2\text{O-ICE}} = 2.6$ Pa) or 180 K (−93 °C) (0.006 Pa). These environments were contained in an insulated foam chamber that permitted ambient air ingress during the fatigue experiment. Additionally, tests were performed in a metal gasket-sealed ultra-high vacuum chamber at room temperature, where prescribed levels of high purity water were introduced to maintain $P_{\text{H}_2\text{O}}$ values at 2.6 and 0.006 Pa. The corresponding $P_{\text{H}_2\text{O}}/f$ values for both the temperature and vacuum system controlled *C-T* tests are identical to the exposure parameters calculated for the low temperature corroded specimen testing. Crack length was determined using compliance.^[64] Fatigue crack growth rate was measured for computer controlled decreasing ΔK with constant K_{\max} of 16.5 MPa $\sqrt{\text{m}}$ and a loading frequency of 20 Hz. The *K*-shed parameter (*C*)^[64] was -0.07 mm^{−1} for the vacuum controlled tests, but varied for temperature controlled testing.

III. RESULTS

Scanning Electron Microscope (SEM) analysis of crack surface marker-bands arrayed about the pit or EXCO localized-corrosion perimeter provides the precise crack formation location and life (N_i to ≈ 20 μm),^[52] as well as the local MSC growth rate.^[23] N_i is computed by comparing the number of applied marker sequences to the number of marker-bands found on the fracture surface; assuming that after formation each loading

sequence marks the fracture surface.* Crack length and

*It is not possible to determine crack formation lives less than the number of baseline cycles associated with the first marker sequence [5,000 for 296 K (23 °C), and 10,000 for 223 K (−50 °C) and 183 K (−90 °C)].

marker-band spacing are measured along local vectors roughly perpendicular to crack formation locations; the vector direction varies for different sites. Marker-band spacing measurement provides the local Δa , which is coupled with the known applied cycles between bands to determine da/dN (secant method^[64]). These growth rates are associated with the mean of the two-total crack lengths which are used to calculate ΔK and K_{\max} . This data collection is detailed elsewhere.^[23,52]

A. Formation

The observed crack formation locations in the primary fracture plane for all controlled pits, stressed at each temperature, are normalized with respect to the mean pit dimensions and plotted in Figure 1.** The 296 K (23 °C)

**62 pits were examined for the 296 K (23 °C) fatigue experiments,^[52] 36 pits for the specimens stressed at 223 K (−50 °C) and 30 pits for the 183 K (−90 °C) case.

data were reported previously and are designated by (◆),^[52] 223 K (−50 °C) data are represented by (■) and 183 K (−90 °C) by (▲); open symbols locate the primary crack formation sites and filled symbols locate secondary sites. Consistent with humid data, crack formation locations for low temperature tests are independent of longitudinal-circumferential position about the pit. Fatigue cracks formed about the center 70 pct (latitudinal position) of the macro-pits. Dividing the regular pit into 7 longitudinal bins and applying a one-sided Kolmogorov–Smirnov (K-S) test ($p = 0.05$) for normality^[65] to each bin establishes that the latitudinal crack formation locations are normally distributed about the equator of the pit. Due to the symmetry of the stresses, the K-S test for each bin is performed on a single data set using the absolute distance from the equator; the quantitative bias in pit formation site towards the top of the sphere is unexplained. Elastic stress concentration factor (k_{t-e}) for a mean-size pit is plotted as a function of perimeter-surface position in Figure 1, where the color scale represents k_{t-e} from near 0 (dark blue) to near 2. This k_{t-e} is defined as the von-Mises effective stress normalized by far-field *L*-direction applied stress, calculated using a 3D monotonic elastic finite element analysis (FEA). Details of this FEA model are reported elsewhere.^[52]

For controlled pits, the mean N_i increases by 30 and 120-fold from humid air at 296 K (23 °C) ($P_{\text{H}_2\text{O}}/f = 80$ Pa s) to the drier 223 K (−50 °C) ($P_{\text{H}_2\text{O-ICE}}/f = 0.13$ Pa s) and 183 K (−90 °C) (3×10^{-4} Pa s) environments, respectively (Table I). The EXCO data demonstrate a significant albeit more modest N_i increase of 7 and 30-fold from 296 K (23 °C) humid to 223 K and 183 K (−50 °C and −90 °C), respectively. Despite these dramatic changes in fatigue crack formation life, the ratio

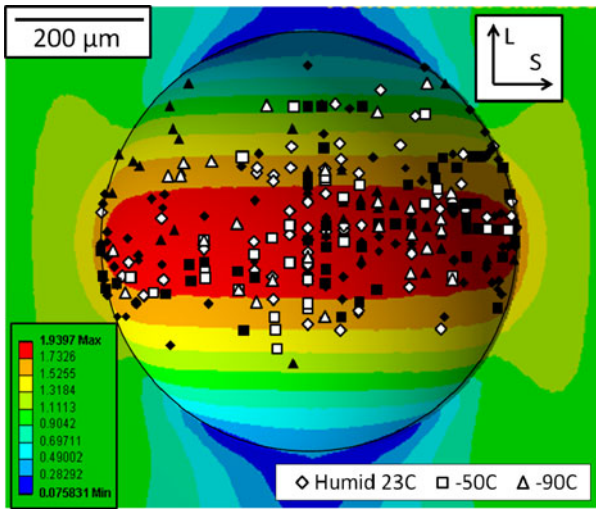


Fig. 1—Values of k_{t-e} from monotonic-elastic FEA analysis of the mean-sized controlled macro-pit loaded along L (maximum $k_{t-e} = 1.94$, red; minimum $k_{t-e} = 0.08$, blue). Data are presented for tests performed at 296 K (23°C) in water saturated N_2 , and in dry N_2 at 223 K and 183 K (−50°C and −90°C). Normalized crack formation site locations are shown, where white symbols represent the locations of the first crack in a given pit and the black symbols show subsequently formed cracks (Color figure online).

of mean N_i to standard deviation (SD) for the 1st formation site (Table I) is ≈ 1.25 and independent of stressing environment. Table II and Figure 1 illustrate that multiple cracks (on average < 2 cracks/pit) form about the perimeter of a single corrosion pit. The effect of adjacent cracks on formation life is not well quantified; as such, mean data are presented for all sites as well as for the first crack to form about a pit. As expected, the mean N_i values for the initial cracks are similar but slightly lower than the mean N_i of the comprehensive data set. The distance from the corrosion perimeter to the first marker-band is similar ($\approx 18 \mu\text{m}$), from 296 K to 223 K (23 °C to −50 °C), but increases two-fold from 223 K to 183 K (−50 °C to −90 °C). The range of measured crack formation lives is reported in Table I; however, note that in each loading environment some pits did not form a crack coincident with the primary fracture surface.

The characteristics of the operative EXCO and pit crack formation sites are temperature independent (Table II); approximately 70 pct of the cracks nucleated from features (5 to 50 μm) that protrude into the corroded area (jut-ins), and 20 pct formed at micro-pits. The remaining cracks form later in life at the pit mouth or other non-geometric features.^[52] Additional crack formation likely occurred on multiple planes that are not coincident with the primary fracture surface; however, it is not possible to distinguish between cracks formed during baseline loading or during the high stress loading at the conclusion of the cold tests.

B. Propagation

Controlled pit and EXCO da/dN values depend on a power law function of crack length (distance from the crack formation site perimeter), as shown in Figure 2 for each environment [296 K (23 °C) results

Table I. Crack Formation Metrics for Corroded 7075-T651 Specimens Fatigued at Constant σ_{max} (200 MPa) and R (0.5) in Various Environments

Corrosion Method (# Pits, Total # of Cracks)	T [K (°C)] ($P_{\text{H}_2\text{O}}/f$)	All Formation Sites			1 st Formation Site	
		1 st Marker Distance (μm)	N_i ($\times 10^3$ cycles)	Mean (Standard Deviation) Ratio of Mean to Standard Deviation	1 st Marker Distance (μm)	N_i ($\times 10^3$ cycles)
Controlled pit (62, 118)	296 (23) (80 Pa s)	18 (12)	50 (40) 1.3	17 (8)	35 (37) 0.9	5-145
Controlled pit (34, 92)	223 (−50) (0.13)	19 (13)	1,370 (1,137) 1.2	18 (11)	1,219 (1,103) 1.1	10-5,400
Controlled pit (28, 56)	183 (−90°C) (3×10^{-4})	28 (24)	4,414 (3,400) 1.3	36 (28)	4,345 (3,627) 1.2	250-15,010
EXCO (3, 4)	296 (23°C) (80)	17 (3)	40 (17) 2.4	16 (3)	42 (21) 2.0	25-65
EXCO (5, 6)	223 (−50) (0.13)	27 (12)	535 (265) 2.0	13 (6)	310 (75) 4.1	235-910
EXCO (3, 5)	183 (−90°C) (3×10^{-4})	18 (6)	1,700 (1,037) 1.6	17 (9)	1,333 (1,041) 1.3	500-2,500

Table II. Crack Formation Characteristics of Corroded 7075-T651 Specimens Fatigued at Constant σ_{\max} (200 MPa), R (0.5) and Various Temperatures

Corrosion Method	Temperature [K (°C)]	Crack Formation Sites Per Pit* Mean (Standard Deviation)	Micro-Topography at Formation Site	
			Jut-in (Pct of Total)	Micro-Pit (Pct of total)
Controlled pit	296 (23)	1.9 (0.9)	73	15
Controlled pit	223 (−50)	2.7 (1.9)	65	24
Controlled pit	183 (−90)	2.0 (1.1)	72	20
EXCO	296 (23)	1.3 (0.6)	100	0
EXCO	223 (−50)	1.2 (0.4)	75	25
EXCO	183 (−90)	1.7 (0.6)	100	0

*The number of crack formation sites on the primary fracture surface.

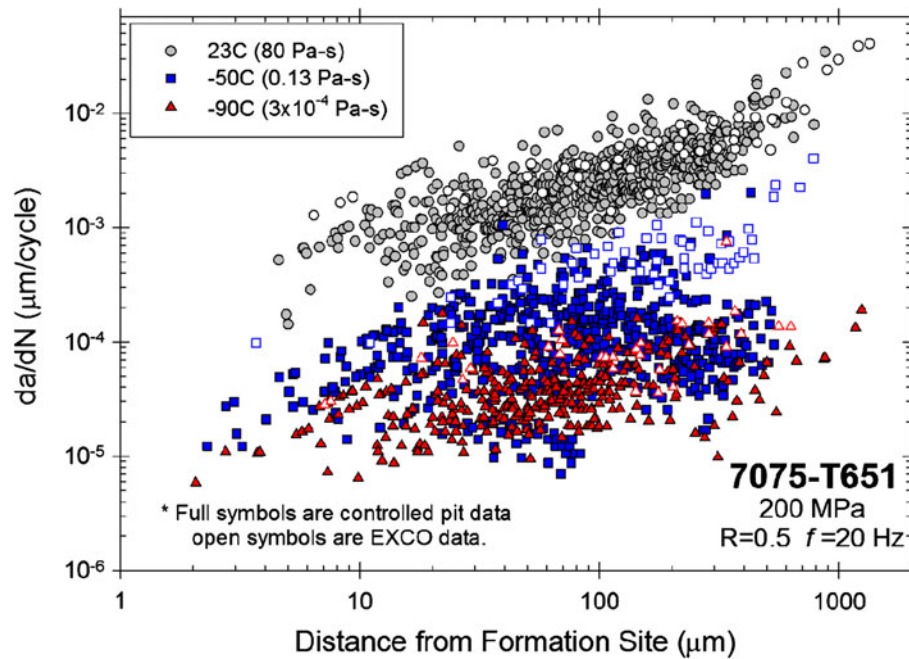


Fig. 2—Fatigue crack growth rate vs crack length data from marker-band analysis of precorroded 7075-T651 specimens tested in room temperature water vapor saturated N_2 and dry N_2 at 223 K and 183 K (−50°C and −90°C). Included are EXCO (open symbols) and controlled pit (closed symbols) data. All tests were performed at $\sigma_{\max} = 200$ MPa, $R = 0.5$ and $f = 20$ Hz. Values of P_{H_2O}/f are listed, assuming equilibrium between vapor and ice at each temperature (Color figure online).

were previously reported^[23]. Critically, for this constant stress condition, and any microstructure-scale crack length, da/dN decreases with decreasing temperature and decreasing-calculated P_{H_2O-ICE} exposure from 80 Pa s to 3×10^{-4} Pa s. Using the controlled pit da/dN for cracks lengths from 45 to 55 μm , the mean and standard deviation in $\mu\text{m}/\text{cycle}$ are 1.8×10^{-3} and 1.0×10^{-3} for humid 296 K (23 °C) loading, 1.4×10^{-4} and 1.2×10^{-4} for 223 K (−50°C), and 3.9×10^{-5} and 2.7×10^{-5} for 183 K (−90 °C).[†] Note

[†]The form of the da/dN distribution in this range was not analyzed, but assuming a normal distribution 2*SD encompasses 95 pct of the data. As such, the maximum da/dN variability about the mean is taken as plus twice the standard deviation divided by the mean times 100 pct.

the order of magnitude decrease in FCG rate from 296 K (23 °C) to 223 K (−50 °C), but only the three-fold decrease from 223 K (−50 °C) to 183 K (−90 °C).

There is excellent correspondence in crack growth rates between the controlled pit and EXCO data at 296 K (23 °C).^[23] This correspondence deteriorated at the lower temperatures and the divergence is particularly acute at crack lengths greater than 150 μm . The leveling or dip in crack growth rate for the low temperature pit data sets [most prominent for 223 K (−50 °C)] corresponds to the onset of a fracture surface morphology change at depths between 150 and 250 μm . The variability at 223 K and 183 K (−50 °C and −90 °C) ($2*SD/\text{mean} = \pm 140$ and ± 172 pct, respectively) is higher than that observed for 296 K (23 °C) (± 110 pct). A power-law trend ($da/dN \sim a^\beta$) fits the humid data ($\beta = 0.61$); however, the high degree of da/dN variability and decrease at ~ 150 to 250 μm preclude fitting single or multiple power-law trends to the 223 K or 183 K (−50 °C or −90 °C) data. These growth rate and variability observations, as well as the crack length dependence and formation feature characteristics, are considered in the Discussion.

1. Stress intensity factor

A common driving force allows comparison of FCG rate data obtained from tests at multiple stress levels on different specimen geometries with different surface-crack initiation site conditions. Elastic stress intensity range is effective in this regard.^[23] For EXCO and controlled pits, the Newman/Raju semi-elliptical surface crack-K solution^[66] is applied to cracks shorter than 500 μm .^[52] Crack size is the measured distance from the specimen surface, the aspect ratio is assumed equal to 1.0, and the tensile and bending stress inputs are computed from the location specific stress gradient due to the 3D pit configuration. A detailed description and justification for these stress intensity calculations is presented elsewhere.^[23] These estimates of K may be systematically low since they fail to account for crack coalescence or continuum-scale plasticity proximate to the crack formation perimeter.

Pit marker-band da/dN vs ΔK data are plotted as data points in Figure 3 for the 296 K, 223 K, and 183 K (23 °C, -50 °C, and -90 °C) environments. The results for the cold environments exhibit the same general dependence on ΔK , and the same-substantial variability, as reported previously for MSC growth at 296 K (23 °C) and reproduced here.^[23] Paralleling the beneficial effect of decreasing temperature on fatigue crack formation, Figure 3 shows a significant decrease in da/dN at any fixed ΔK as temperature decreases from 296 K to 223 K (23 °C to -50 °C), but less severe decrease from 223 K to 183 K (-50 °C to -90 °C). Table III reports the mean and standard deviation of da/dN for each temperature over the specified ΔK ranges, the \pm percent variability ($2 \cdot \text{SD}/\text{mean}$) about the mean, and number of data points used in the calculations. There is a 12-fold decrease in mean growth rate from 296 K to 223 K (23 °C to -50 °C) at lower stress intensities (≈ 0.75 and 1 $\text{MPa}\sqrt{\text{m}}$); this reduction is magnified to 17-fold and 34-fold at $\Delta K \approx 2$ and 3 $\text{MPa}\sqrt{\text{m}}$, respectively. A decrease in temperature from 223 K to 183 K (-50 °C to -90 °C) results in a modest additional reduction (3 to 6-fold) of the mean da/dN at each ΔK level. Table III suggests that the variability is consistent (± 70 to 130 pct variation) for all controlled pit cases, except for the high variation (± 180 to 380 pct) for 223 K (-50 °C) data at ≈ 2 and 3 $\text{MPa}\sqrt{\text{m}}$ (Figure 3).

Also included in Figure 3 are trend line representations of $C-T$ FCG results for 7075-T651 stressed at $P_{\text{H}_2\text{O}}/f$ (or $P_{\text{H}_2\text{O-ICE}}/f$) values of 120, 0.13, 3×10^{-4} , and $\sim 1 \times 10^{-7}$ Pa s. (The red and blue dotted lines are extrapolations discussed in subsequent sections.) Water vapor pressure is controlled either by varying temperature, and assuming the vapor pressure of H_2O above ice, or introduction of controlled levels of high purity water into ultra-high vacuum at 296 K (23 °C). The FCG rates for vacuum controlled environments at 296 K (23 °C) decrease with each decrease in $P_{\text{H}_2\text{O}}/f$, but are constant for the two low exposures which include 3×10^{-4} Pa s and $\sim 1 \times 10^{-7}$ Pa s. In contrast the temperature controlled $C-T$ results for 0.13 [223 K (-50 °C)] and 3×10^{-4} Pa s [183 K (-90 °C)] are equal and slightly below the 296 K (23 °C) ultra-high vacuum trend line. The lack of correspondence between the

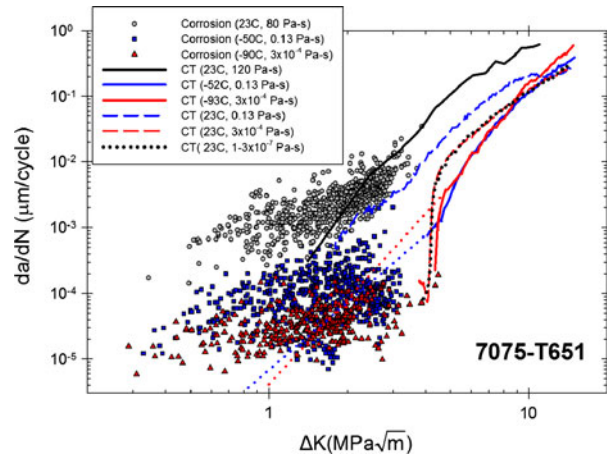


Fig. 3—Fatigue crack growth rate vs ΔK data from marker analysis of 7075-T651 pit specimens tested at $\sigma_{\text{max}} = 200$ MPa and $R = 0.5$ in water saturated N_2 at 296 K (23°C), and dry N_2 at 223 K and 183 K (-50°C and -90°C). Also included are high constant K_{max} (16.5 $\text{MPa}\sqrt{\text{m}}$)-decreasing ΔK relationships obtained from $C-T$ specimen tests conducted at $P_{\text{H}_2\text{O}}/f$ of 120, 0.13, and 3×10^{-4} Pa s. Water vapor pressure is controlled by either lowering temperature or introduction of high purity water into a high vacuum system at 23°C (Color figure online).

temperature and vacuum controlled $C-T$ data, and the temperature dependence of the marker-band data, have important implications for understanding low temperature fatigue, as considered in the Discussion.

For fatigue at 296 K (23 °C), controlled pit and EXCO growth rates are well aligned, as shown in Figure 4, where all marker-band da/dN data are plotted vs ΔK .^[23] Quantitative comparison of individual data sets, with the combined set of all 296 K (23 °C) data (Table III), shows similar mean da/dN values and lower (or equal) variability for each ΔK level. However, this correspondence deteriorates with decreasing temperature (Figure 4). Despite testing at identical $P_{\text{H}_2\text{O-ICE}}/f$ values, the low temperature EXCO results slightly exceed controlled pit data at $\Delta K \approx 0.75$ and 1 $\text{MPa}\sqrt{\text{m}}$; this deviation is more pronounced at 2 and 3 $\text{MPa}\sqrt{\text{m}}$ (Table III). The excellent correspondence between all 296 K (23 °C) data suggests that the estimates of the mechanical driving force for the pits and EXCO geometries are sound. As such, the differences observed for the low temperature data sets likely reflect either a role of H-charging during the corrosion process, or differences in formation feature associated with pit vs EXCO micro-topography. Extensive fracture surface microscopy did not reveal evidence of the latter.^[52]

C. Fracture Surface Morphology

Fatigue crack surface morphology depends on stressing temperature, specimen corrosion condition, applied stress intensity, and crack length. For controlled pit fatigue at 296 K (23 °C) (humid), Figure 5 shows flat and smooth features which on-average extend 40 to 80 μm from the pit perimeter, then transition to a rougher veined morphology with flat features interspersed ($a-b$). The latter is consistent with 296 K (23 °C) (humid) $C-T$ fracture surface morphologies. The flat

Table III. Statistical Parameters for Crack Growth Rate Data in Figs. 3 and 4 for 7075-T651 Corroded Specimens Fatigued at Various Stress Levels and Temperatures

Specimen Type Temperature K (°C)	Range of ΔK Over Which Data Are Collected (MPa \sqrt{m})			
	0.7-0.8	0.95-1.05	1.95-2.05	2.95-3.05
	<i>da/dN</i> Sample Size Mean ($\mu\text{m}/\text{cycle}$) Standard Deviation ($\mu\text{m}/\text{cycle}$) \pm Pct Variation			
Controlled pit 296 (23)	16 1.0×10^{-3} 3.5×10^{-4} 70	26 1.2×10^{-3} 7.3×10^{-4} 126	40 2.8×10^{-3} 1.6×10^{-3} 116	10 1.1×10^{-2} 4.8×10^{-3} 86
Controlled pit 223 (-50)	21 8.4×10^{-5} 3.7×10^{-5} 88	24 9.8×10^{-5} 5.4×10^{-5} 108	30 1.2×10^{-4} 1.1×10^{-4} 180	9 3.2×10^{-4} 6.1×10^{-4} 378
Controlled pit 183 (-90)	21 2.5×10^{-5} 1.7×10^{-5} 132	19 2.8×10^{-5} 1.5×10^{-5} 108	16 5.0×10^{-5} 2.6×10^{-5} 104	6 5.5×10^{-5} 3.2×10^{-5} 118
EXCO 296 (23)	1 1.9×10^{-3} ? ?	3 1.8×10^{-3} 3.1×10^{-4} 34	6 3.4×10^{-3} 1.1×10^{-3} 68	6 6.6×10^{-3} 1.9×10^{-3} 58
EXCO 223 (-50)	1 9.8×10^{-5} ? ?	3 2.0×10^{-4} 6.9×10^{-5} 70	6 6.2×10^{-4} 1.7×10^{-4} 56	4 7.3×10^{-4} 2.0×10^{-4} 54
EXCO 183 (-90)	? ? ? ?	4 6.9×10^{-5} 2.2×10^{-5} 64	4 7.0×10^{-5} 7.5×10^{-6} 22	2 1.5×10^{-4} 4.8×10^{-5} 64
All data 296 (23)	17 1.2×10^{-3} 4.0×10^{-4} 70	29 1.3×10^{-3} 7.4×10^{-4} 116	46 3.0×10^{-3} 1.6×10^{-3} 104	16 9.3×10^{-3} 4.0×10^{-3} 86
Controlled pit/EXCO 223 (-50°C)	22 8.5×10^{-5} 3.6×10^{-5} 86	27 1.1×10^{-4} 5.9×10^{-5} 112	36 1.8×10^{-4} 1.0×10^{-4} 222	13 4.4×10^{-4} 5.4×10^{-4} 260
Controlled pit/EXCO 183 (-90°C)	21 2.5×10^{-5} 1.7×10^{-5} 132	23 3.5×10^{-5} 2.2×10^{-5} 128	20 5.4×10^{-5} 2.5×10^{-5} 92	8 7.9×10^{-5} 5.5×10^{-5} 140

?—Insufficient *da/dN* data for analysis.

regions, present at 85 pct of the initiation sites, are speculatively characteristic of cracking through a cyclically developed and H embrittled dislocation cell structure.^[42,47] The fracture surface morphologies of the 223 K (-50 °C) (Figure 6) and 183 K (-90 °C) (Figure 7) specimens are similar to one another, but much different from the 296 K (23 °C) humid results. Each low temperature test exhibits a broad-flat region surrounding the pit and extending about 150 to 250 μm inward (Figures 6(a) and (b), and 7(a)). Higher magnification analyses

(Figures 6(c) and (d), and 7(d)) show a sub-micron scale roughness on these flat surfaces, contrary to the smooth flat regions typical of 296 K (23 °C) humid specimens (Figure 5(c)). The cold specimen morphology beyond 150 to 250 μm exhibits facet features (Figures 6(a) and (b), and 7(c)) on the order of the S-direction grain size (8 to 19 μm). Such features are also observed in *C-T* specimens at ΔK below ≈ 4 MPa \sqrt{m} for $P_{\text{H}_2\text{O-ICE}}/f = 0.13$ and 3×10^{-4} Pa s and $P_{\text{H}_2\text{O}}/f = 3 \times 10^{-4}$ and 1×10^{-7} Pa s. Notably, the 0.13 Pa s vacuum system

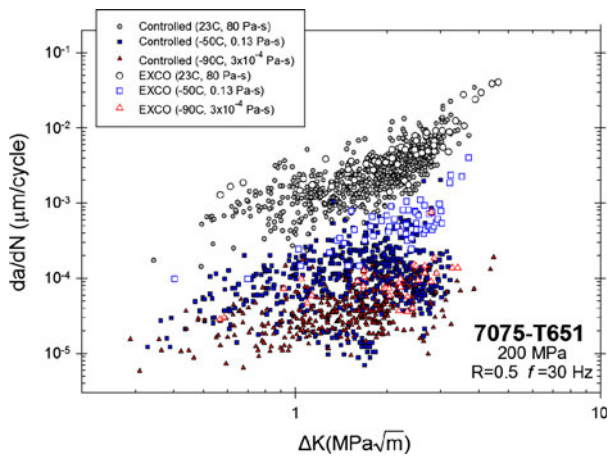


Fig. 4—Fatigue crack growth rate vs ΔK data from marker-band analysis of 7075-T651 EXCO corroded, and controlled pit specimens, tested at $\sigma_{\max} = 200$ MPa and $R = 0.5$ in water saturated N_2 at 296 K (23°C), and dry N_2 at 223 K and 183 K (−50°C and −90°C) (Color figure online).

controlled C - T specimen did not exhibit such features.^[67] These features are assumed to be oriented parallel to slip planes or the slip band-matrix interface suggesting SBC. This assumption is consistent with: (1) results for Al-Li-Cu, Al-Cu-Mg, and Al-Zn-Mg-Cu alloys with shearable atom clusters or precipitates tested in ultra-high vacuum, where similar facet features were aligned within 15° of the {111} slip plane,^[33,42,45] and (2) the finding that slip band cracking can occur even in peak-aged alloys (*i.e.*, 7075) with Cu-content below about 1.6 wt pct.^[68,69] At roughly 1,500 μm , the fracture surface characteristics transition from organized crystallographic cracking to features typical of high- ΔK plasticity-based cracking (Figures 7(a) and (b)), where the slip is homogenized across multiple slip systems.

The EXCO 223 K and 183 K (−50 °C and −90 °C) fatigue crack surface morphologies are similar to one another, but distinct from controlled pit results. As shown in Figure 8, an EXCO specimen stressed at 223 K (−50 °C) exhibits features consistent with 296 K (23 °C) (humid) crack surfaces for both pit and EXCO surface conditions, with interspersed features similar to low temperature controlled pit specimens. Similarities between EXCO 223 K and 296 K (−50 °C and 23 °C) fatigue crack surface features are consistent with growth rate similarity in Figure 4. Figure 8(b) illustrates that the area proximate to the fracture surface is a mix of the smooth-flat features (humid; Figure 5(c)) and flat fine-roughness features (cold; Figures 6(c) and (d), and 7(d)). Isolated features in some specimens suggest sporadic slip-band like cracking at a ≈ 500 μm , but a distinct transition to a slip-band-based morphology is not observed. Figures 5, 6, 7, and 8 provide examples, but the reported trends are based on a comprehensive analysis of ≈ 140 pits.

IV. DISCUSSION

Decreasing loading temperature from 296 K to 223 K and 183 K (23 °C to −50 °C and −90 °C) substantially increases the fatigue resistance of 7075-T651. Experimental results establish this strong temperature dependence

for: fatigue crack formation (Table I), microstructure-scale growth (Figures 2, 3, 4), and long crack growth (Figure 3), the former two associated with pre-corrosion damage. These data provide a novel foundation for both engineering prognosis,^[1,2,8–10] including validation of models proposed to describe MSC rates,^[1,53–57] and mechanistic understanding of fatigue crack tip damage from plasticity-H interaction. This Discussion first examines the use of water vapor pressure as a proxy to predict the effect of temperature on da/dN vs ΔK . Then the elements of crack tip hydrogen embrittlement, including both pit perimeter H from corrosion and crack tip H produced by water vapor reaction during stressing, are considered to explain the effects of temperature on N_i , $(da/dN)_{\text{MSC}}$, and changes in crack surface morphology unique to the pit-to-crack transition regime. Finally, experimental results and understanding are discussed in the context of including temperature-environment effects in next-generation fatigue prognosis at the length scale set by localized corrosion damage.

A. Temperature- $P_{\text{H}_2\text{O}}/f$ Dependence of Crack Growth

1. Role of temperature dependent $P_{\text{H}_2\text{O}}/f$

The effect of water-bearing gas environments on da/dN is understood through localized crack tip process zone hydrogen environment embrittlement (HEE).^[30–32] For room temperature loading where the water vapor pressure is below the condensation level, da/dN is well described by a complex function of bulk $P_{\text{H}_2\text{O}}/f$.^[34,48–50,70] This section discusses the efficacy of using water vapor pressure as a simple proxy to predict the effect of temperature on da/dN vs ΔK .

For cold environment applications, water vapor pressure can be either in equilibrium with ice frozen on a metal surface, or inherent in the high altitude environment; with the specific situation dependent on location in the airframe and meteorological conditions.^[71] Considering the former, the $P_{\text{H}_2\text{O}}$ about the crack mouth is more relevant to mass transport and reaction modeling of da/dN than the global-bulk level. At temperatures above 273 K (0 °C) where the only stable phase is water vapor, the bulk and crack mouth levels are identical. However, below 0 °C an ice layer forms to fix the crack mouth $P_{\text{H}_2\text{O}}$ to the ice-vapor equilibrium pressure at a given temperature. As such, the temperature controlled ice-vapor equilibrium $P_{\text{H}_2\text{O}}$ is assumed to represent the local crack mouth environment and these values were listed in Figures 2, 3, and 4.^[63] For high altitude flight, low bulk-environment $P_{\text{H}_2\text{O}}$ may preclude ice formation at a given temperature. In such cases $P_{\text{H}_2\text{O-ICE}}$ represents a conservative upper bound on the airframe environment for operations above the cloud line where either: (1) ice was not formed during lower altitude-higher humidity flight segments, or (2) sublimation of the ice occurred.^[72] Here, the actual-lower bulk $P_{\text{H}_2\text{O}}$ from meteorological information can be used in a da/dN (K , K_{\max} , $P_{\text{H}_2\text{O}}/f$) model and could be lowered further by water molecule adsorption on Al. The presence of ice on precorroded MSC and C - T specimen surfaces in the current fatigue experiments suggests that there was sufficient bulk $P_{\text{H}_2\text{O}}$ contamination in the N_2 cooled chamber to form ice. A first

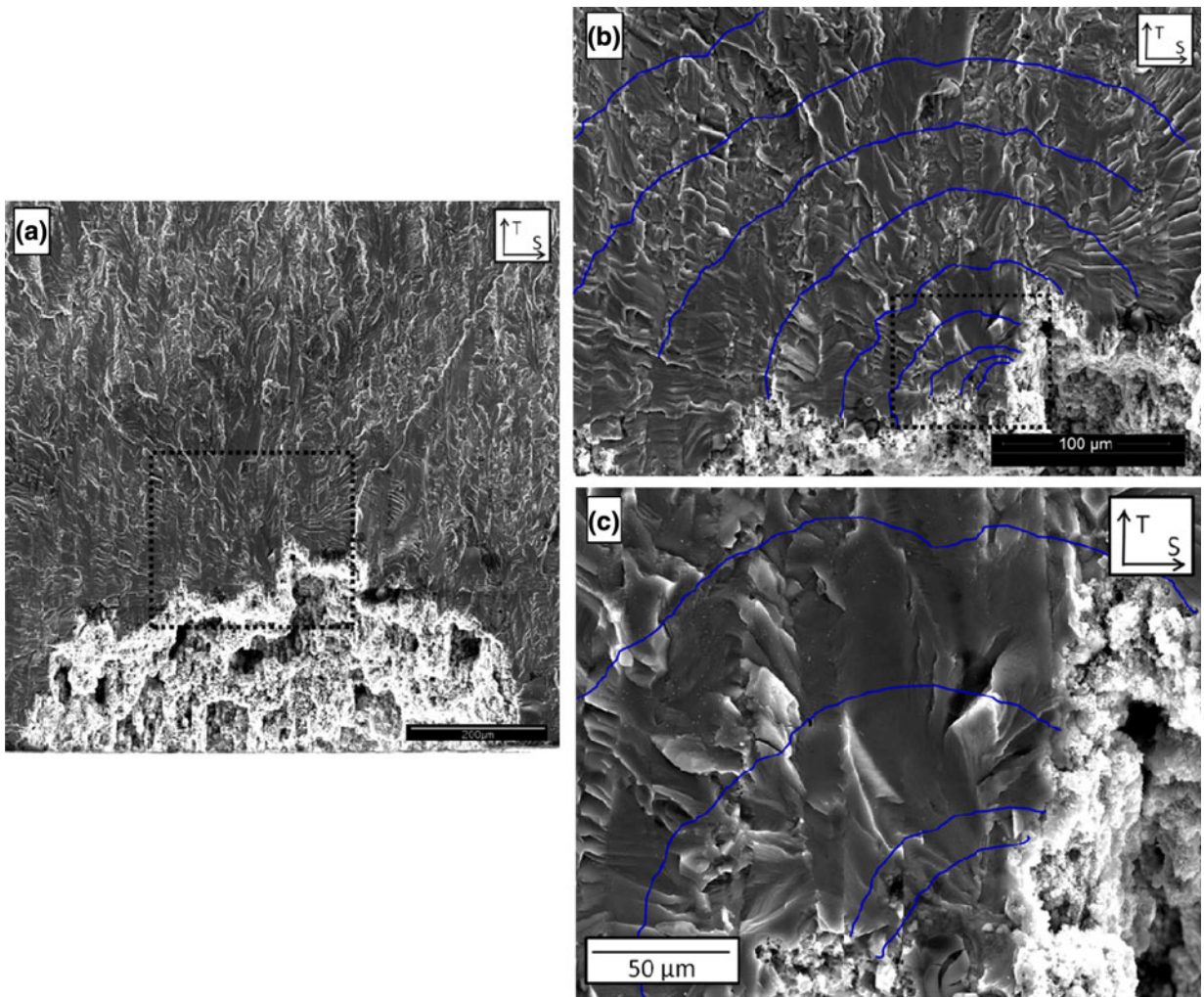


Fig. 5—Fractographs of the T - S fracture plane of a 7075-T651 controlled pit specimen stressed in water saturated N_2 at 296 K (23°C). The blue lines in (b) and (c) highlight marker-bands quantifying crack progression from the pit perimeter in the bottom of each image. The dashed box in the low magnification image (a) denotes the crack formation area shown at higher magnification in (b) and further magnified in (c). Crack growth is from bottom to top (Color figure online).

hypothesis is that the reduced da/dN with decreasing temperature below 273 K (0 °C) is largely explained by the reduction in P_{H_2O} above ice.

The role of P_{H_2O}/f is directly evaluated by comparing the vacuum-system (296 K (23 °C)) controlled vs N_2 -chamber/temperature controlled environmental C - T -crack growth rates (Figure 3). The lack of da/dN correspondence at constant P_{H_2O}/f and ΔK suggests that the water vapor hypothesis is overly simplistic. For example, at $\Delta K = 5 \text{ MPa}\sqrt{\text{m}}$, da/dN at 0.13 Pa s is $3.2 \times 10^{-2} \text{ }\mu\text{m/cycle}$ at 296 K (23 °C) but 10-fold slower ($3.3 \times 10^{-3} \text{ }\mu\text{m/cycle}$) at 221 K (−52 °C) and the same P_{H_2O}/f . The da/dN at 0.0003 Pa s is $1.3 \times 10^{-2} \text{ }\mu\text{m/cycle}$ at 296 K (23 °C) but $4.8 \times 10^{-3} \text{ }\mu\text{m/cycle}$ at 180 K (−93 °C). Similar differences are apparent at other ΔK levels in Figure 3. Moreover, the C - T experiments conducted at 221 K and 180 K (−52 °C and −93 °C) exhibit apparent threshold stress intensity ranges at $\approx 4.5 \text{ MPa}\sqrt{\text{m}}$, while the 0.13 Pa s experiment at 296 K (23 °C) shows that the threshold is below $2 \text{ MPa}\sqrt{\text{m}}$. While the temperature-induced reduction in P_{H_2O} above ice significantly contributes to improved fatigue resistance, Figure 3 shows that this environmental parameter cannot

be exclusively employed to quantify the effect of temperature on fatigue. Additional temperature-dependent factors are considered below.

2. Understanding temperature dependent mechanisms

The intrinsic properties of aluminum alloys are temperature dependent^[73,74] due to variations in interatomic forces (for E) and dislocation motion (for σ_{ys} , K_{IC}).^[75] Such changes result in the reduction of the plastic strain range-based crack tip mechanical driving force as temperature decreases for fixed-applied ΔK . However, calculations using temperature dependent E and σ_{ys} result in only a 12 pct reduction in cyclic crack tip opening displacement (ϕ_c) from 250 K to 183 K (−23 °C to −90 °C)^[53].[‡] This

[‡]Assuming that ϕ_c is a proper crack tip driving force, then a reasonable continuum growth rate relationship is $da/dN \sim \phi_c \sim \Delta K^2/(\sigma_{ys}^*E)$.^[76] Using σ_{ys} and E values for 7075-T651 at 223 K (−50 °C) ($\sigma_{ys} = 521 \text{ MPa}$, $E = 75,797 \text{ MPa}$) and 183 K (−90 °C) ($\sigma_{ys} = 526 \text{ MPa}$, $E = 78,528 \text{ MPa}$),^[74] the ratios of ϕ_c at 296 K (23 °C) to ϕ_c at 223 K (−50 °C) or 183 K (−90 °C) are 0.92 and 0.88, respectively.

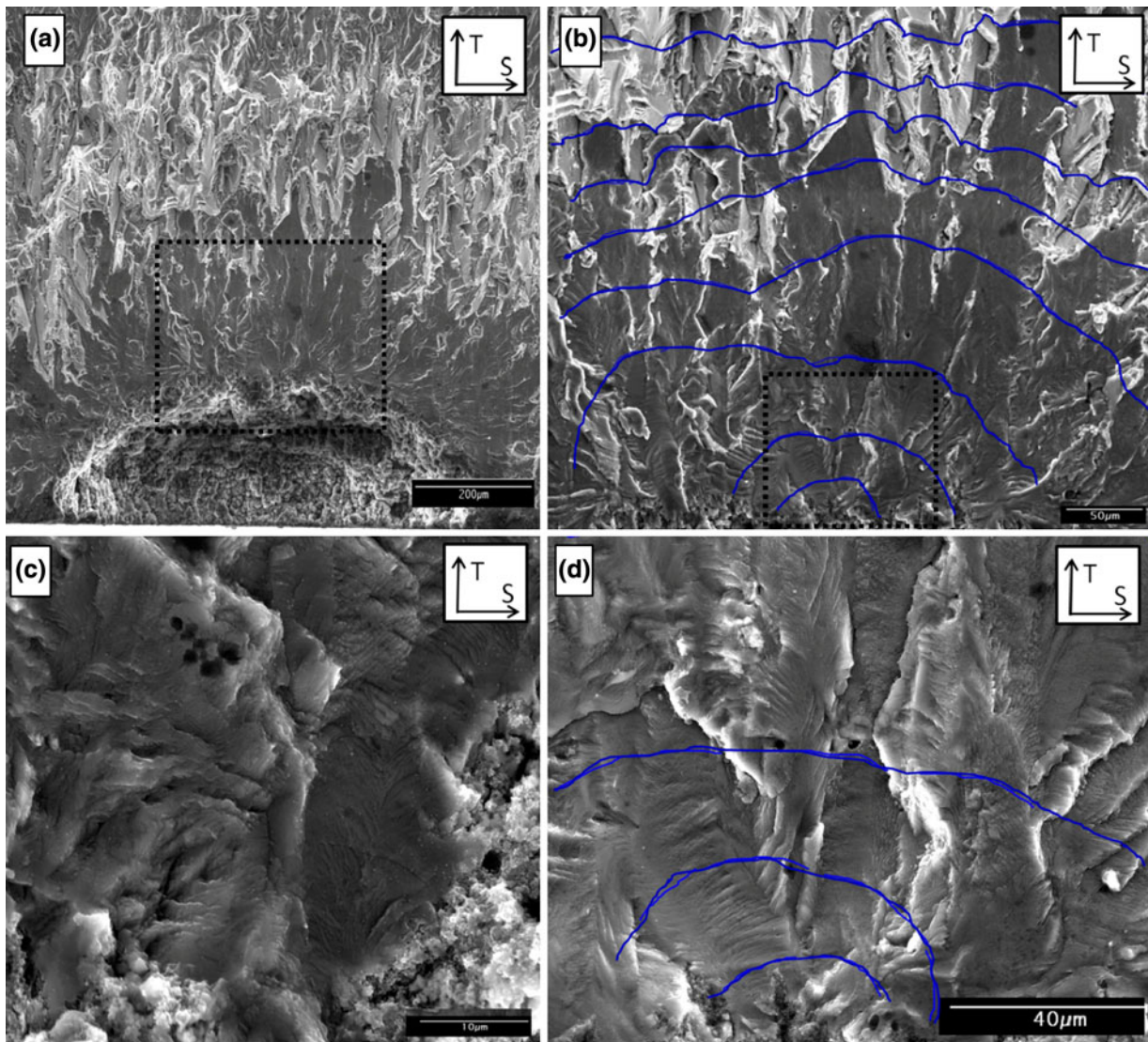


Fig. 6—Fractographs of the T - S fracture plane of a 7075-T651 controlled pit specimen stressed in dry N_2 at 223 K (-50°C). The dashed box in the low magnification image in (a) denotes the region shown at higher magnification in (b) and further magnified in (c). The blue lines highlight marker-bands and crack growth is from bottom to top. The high magnification images in (c) and (d) demonstrate the flat micro-roughness regions ((d) is a separate pit) (Color figure online).

effect fails to account for the strong reductions in da/dN unique to the low temperature conditions in Figure 3, but does explain why C - T data for each cold temperature are somewhat below the ultra-high vacuum results measured at 296 K (23°C).

It is useful to establish the temperature dependence of each stage of the H-embrittlement processes to enable mechanistic understanding of the complex relationship between $P_{\text{H}_2\text{O}}/f$, temperature, and da/dN . Isothermal C - T experiments at 296 K (23°C), summarized in Figure 9 for the present lot of 7075-T651 stressed at ΔK of 3.0 $\text{MPa}\sqrt{\text{m}}$ (\blacksquare , \blacklozenge) align with the well-known three-stage $P_{\text{H}_2\text{O}}/f$ dependence of da/dN . FCG rate is governed by one or more of the rate-limiting processes associated with water molecule transport to the crack tip, surface reaction to produce atomic H on crack tip surfaces, and H diffusion into the crack tip process zone.^[34,48–50,70] In the low exposure regime with $P_{\text{H}_2\text{O}}/f$

increasing from ultra-high vacuum (10^{-7} Pa s), there is insufficient supply of water molecules such that FCG rate is exclusively governed by mechanical damage accumulation (*i.e.*, crack tip plasticity). In the intermediate exposure regime, da/dN is directly proportional to the surface concentration of H (C_{HS}) resulting from crack tip surface reaction with water vapor and thus directly proportional to $P_{\text{H}_2\text{O}}/f$.^[34,47–51] At room temperature surface reaction and diffusion are rapid in this da/dN regime, thus C_{HS} is limited by the geometrically impeded flow of water molecules from the crack mouth to the lower pressure region established at the crack tip.^[34,51] Above a saturation value $(P_{\text{H}_2\text{O}}/f)_{\text{sat}}$ (0.01 Pa s for this material and ΔK), and associated $(da/dN)_{\text{cf-sat}}$, growth rates are mildly dependent on $P_{\text{H}_2\text{O}}/f$. The rate limiting mechanism change responsible for the transition from the intermediate to high exposure regime is not fully established, but may include: multiple-saturated

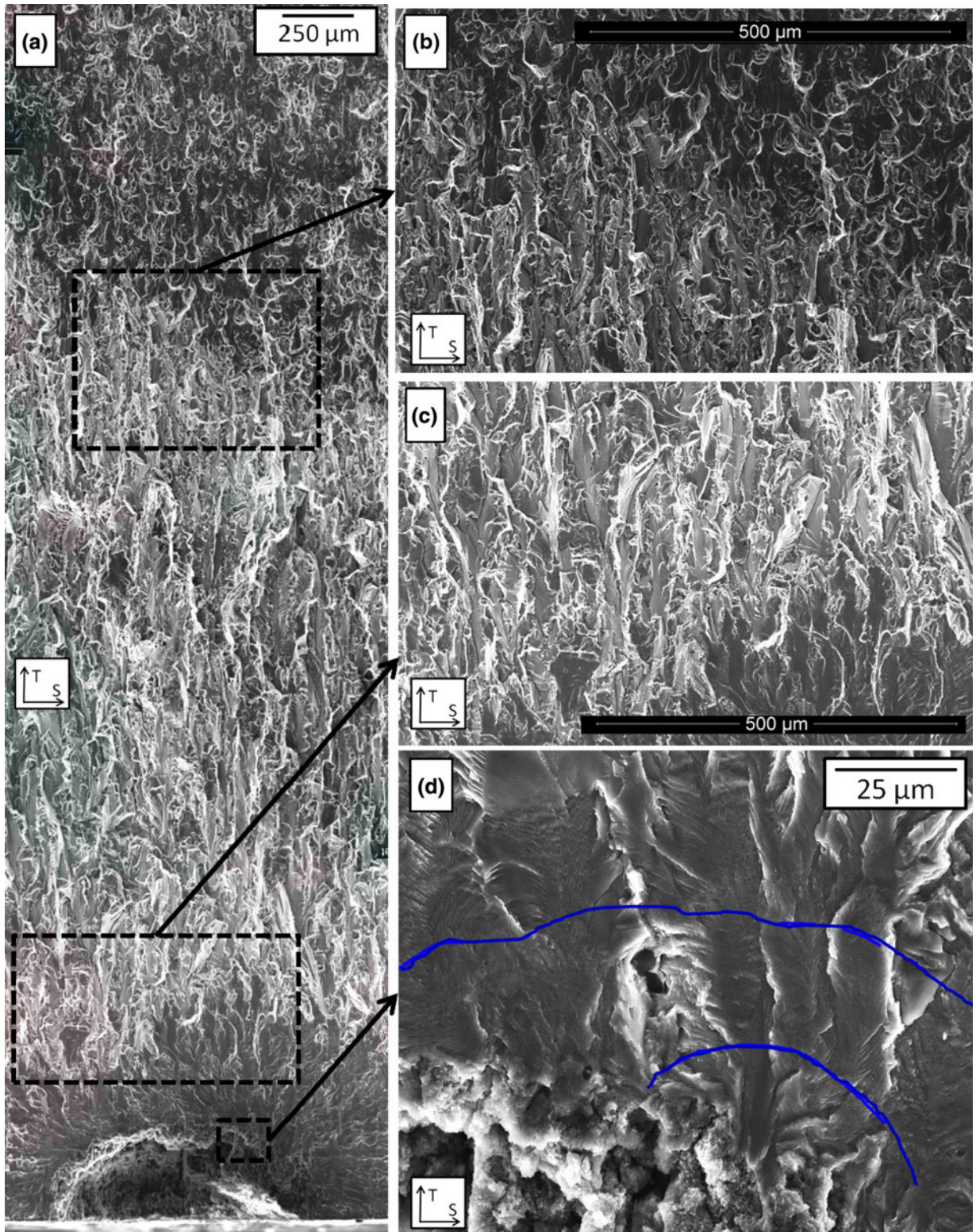


Fig. 7—Fractographs of the *T-S* fracture plane of a 7075-T651 controlled pit specimen stressed in dry N₂ at 183 K (−90°C). An overview of pit to crack progression is shown in (a) where the dashed boxes highlight the formation region in (d), the transition slip-band like morphology in (c) and the transition to high plasticity cracking in (b). Crack growth is from bottom to top and the blue lines denote marker-band locations (Color figure online).

surface reactions, H diffusion rate limitation, or water condensation due to crack tip curvature.^[34,51,77] The rate-limiting step paradigm provides a more complete

basis to examine the temperature dependence of da/dN in the context of H-embrittlement; this assumes that temperature dependent temperature dependent

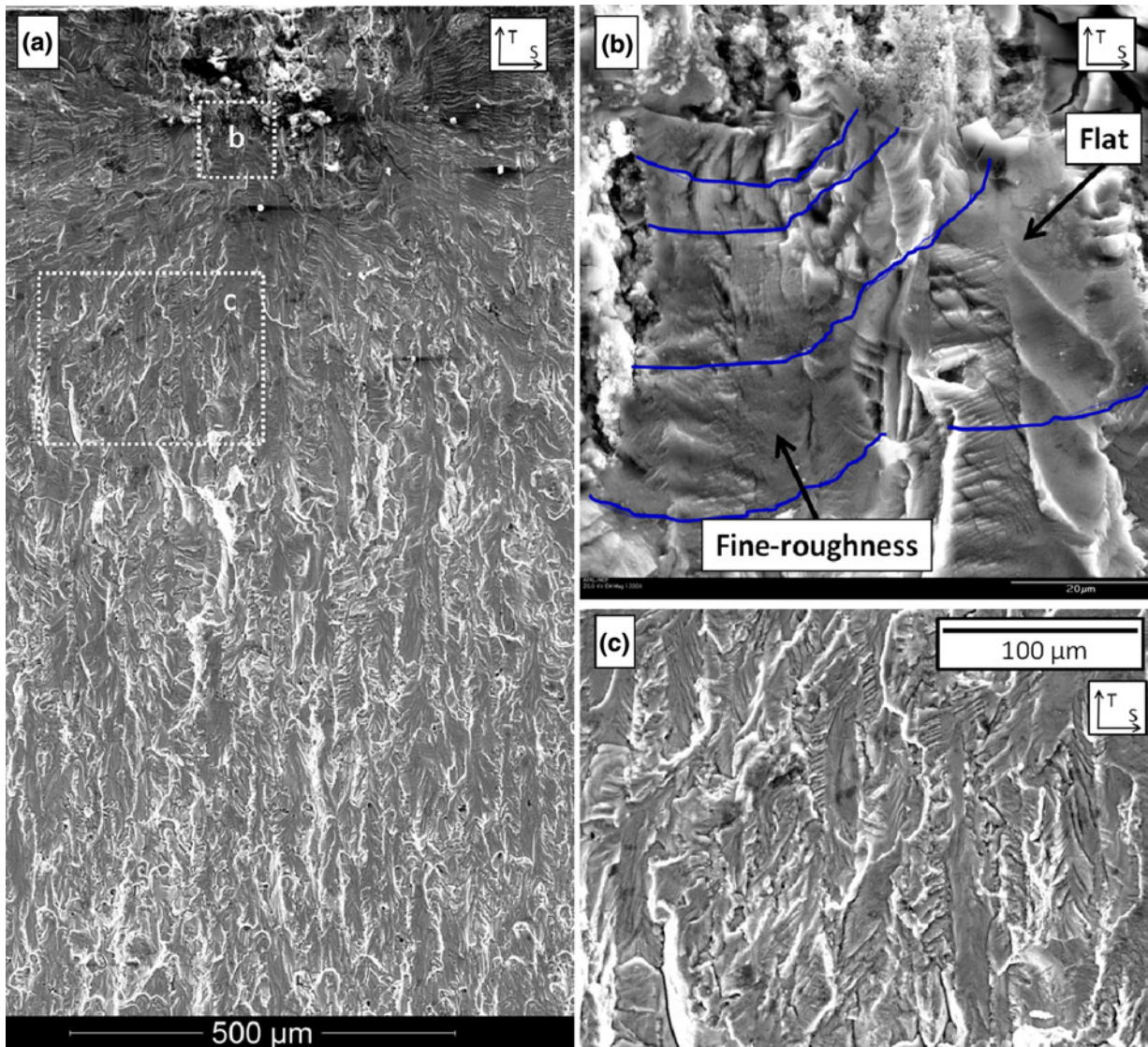


Fig. 8—Fractographs of the T - S fracture plane of a 7075-T651 EXCO corroded fatigue specimen stressed in dry N_2 at 223 K (-50°C). An overview of crack progression from the EXCO-pit (top) is shown in (a), the dashed boxes highlight the formation region in (b), and show a lack of features that would indicate slip-band like cracking in (c). Crack growth is from top to bottom and the blue lines denote marker-band locations (Color figure online).

plasticity-damage accumulation is a secondary factor.^[78] The temperature dependencies of molecular flow, crack tip surface reactions, and H diffusion are considered below.

Wei *et al.* solved the coupled differential equations for impeded molecular (Knudsen) flow of water vapor to the crack tip followed by surface reaction to form H, assuming Langmuir kinetics.^[48–50] The total FCG rate plotted in Figure 9 is the sum of an inert environment growth rate $[(da/dN)_{\text{intrinsic}}]$ and environmental component $[(da/dN)_{\text{cf}}]$, which linearly depends on exposure in the Knudsen flow-rate limited regime below $(P_{\text{H}_2\text{O}}/f)_{\text{sat}}$:

$$\left(\frac{da}{dN}\right)_{\text{cf}} = \frac{P_{\text{H}_2\text{O}}}{f} \left[436 \frac{\beta}{\alpha N} f(R) \frac{\sigma_{\text{ys}}^2}{kTE^2} \left(\frac{T}{M}\right)^{\frac{1}{2}} \right] \left(\frac{da}{dN}\right)_{\text{cf-sat}} \quad [1]$$

where f is frequency, N is the density of surface reaction sites (10^{19} Al atoms/ m^2), k is the Boltzman constant, T is temperature in degrees-Kelvin, E is Young's modulus, M is the molecular weight of water vapor, $f(R)$ is a function of stress ratio, and α and β are empirical constants related to surface roughness and flow, respectively. The model is not fully predictive, since no failure criterion for H-enhanced crack advance is included. Rather, predictions are scaled to fit the measured crack growth rate at the transition between intermediate and high exposure regime, $(da/dN)_{\text{cf-sat}}$. This model for the Knudsen flow regime has been validated using room temperature experiments with controlled water vapor pressures at intermediate exposures and higher ΔK levels,^[47–50] as confirmed and extended to a low ΔK of $3.0 \text{ MPa}\sqrt{\text{m}}$ (■) in Figure 9. Equation [1] gives the functional dependence of da/dN on $P_{\text{H}_2\text{O}}/f$ and T in

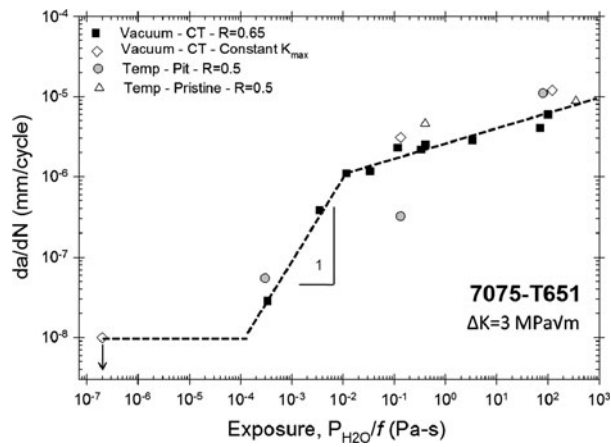


Fig. 9—The exposure dependence of fatigue crack growth rate for the current heat of 7075-T651 at $\Delta K = 3.0 \text{ MPa}\sqrt{\text{m}}$. Long crack *C-T* results at fixed *R* of 0.65 (■), and with a constant K_{max} -decreasing ΔK protocol (◇), are based on controlled-pure water vapor pressure in a UHV system at 296 K (23°C).^[1] MSC growth rates are plotted for pitted specimens stressed at *R* of 0.5, with varying temperature from 296 K to 183 K (23°C to -90°C) (●; see Table III; Fig. 3), and for pristine specimens stressed at *R* of 0.5 with temperature of 296 K or 223 K (23°C or -50°C) (△)^[23,91].

the intermediate exposure regime where: (a) sufficient water is present to facilitate embrittlement (b) H diffusion does not limit da/dN , and (c) da/dN is directly proportional to $P_{\text{H}_2\text{O}}/f$.

The temperature dependent terms in Eq. [1] were evaluated to determine the relative influence of each on da/dN , compared to changing $P_{\text{H}_2\text{O}}$. Temperature and temperature dependent material properties (E , σ_{ys}) are combined to $\gamma = (\sigma_{\text{ys}}/E)^2 * (T^{0.5}/T)$. The $P_{\text{H}_2\text{O}}$ and γ values are normalized by 296 K (23°C) data, and plotted vs temperature in Figure 10. This plot shows that the effect of temperature on da/dN_{cf} is primarily accounted for by reduced $P_{\text{H}_2\text{O}}$ above ice, with the Knudsen flow parameters combining to a mildly rising value of γ with falling temperature. The effect of the variation in crack path roughness between humid and cold specimens shown in Figures 6, 7, and 8 suggests that α and β vary with temperature; however, the magnitude of these changes is not clear. Provided that changes in α and β are minor in the context of Figure 10, the temperature dependence of the Knudsen flow model is captured by $P_{\text{H}_2\text{O}}/f$ from the ice-vapor equilibrium. As such the lack of growth rate correspondence at constant $P_{\text{H}_2\text{O}}/f$ in Figure 3, and the presence of 223 K (-50°C) $P_{\text{H}_2\text{O-ICE}}/f$ da/dN values above $(da/dN)_{\text{cf-sat}}$ in Figure 9, clearly demonstrate that molecular flow is not solely governing the temperature dependence of da/dN .

Temperature dependent reductions in H₂O adsorption, H₂O-Al surface reaction rate, and/or reaction extent, may explain low temperature da/dN below the levels observed in Figure 3 for identical $P_{\text{H}_2\text{O}}/f$ at 296 K (23°C). Wei *et al.* modeled the H-environment affected contribution to fatigue crack growth when surface reaction is rate limiting.^[51,79]

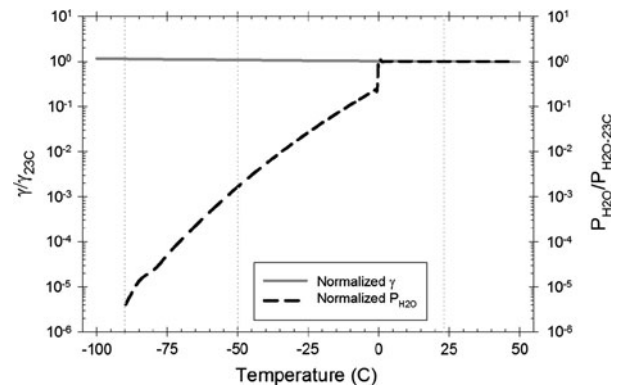


Fig. 10—A plot of the temperature dependent Knudsen flow parameters, $\gamma = (\sigma_{\text{ys}}/E)^2 * (T^{0.5}/T)$, and water vapor pressure ($P_{\text{H}_2\text{O}}$) vs temperature, each normalized by values at 296 K (23°C). For all temperatures above the freezing point, the $P_{\text{H}_2\text{O}}$ for 296 K (23°C) and 85 pct relative humidity is plotted. For temperatures below the freezing point, $P_{\text{H}_2\text{O}}$ is set by the equilibrium water vapor pressure above ice.

$$\left(\frac{da}{dN}\right)_{\text{cf}} = A \left(1 - \exp\left[\frac{-k_c P_{\text{H}_2\text{O}}}{f}\right]\right) \quad [2]$$

$$k_c = k_{\text{co}} \exp\left[\frac{-E_s}{RT}\right]$$

where A is the difference between the maximum-environmentally assisted and inert-mechanical growth rates, $P_{\text{H}_2\text{O}}$ is the water vapor pressure at the crack mouth, k_c is the rate of water vapor reaction with Al to produce H, k_{co} is reaction rate constant, E_s is activation energy for the controlling surface reaction sequence, and R is the gas constant. It is not possible to estimate the temperature dependence of $(da/dN)_{\text{cf}}$ because the model represented in Eq. [2] does not account for the multi-step reactions necessary to produce H on a newly formed crack surface,^[51,80] and effective values of k_{co} and E_s ^[81] for the multiple surface reactions, adsorption, and absorption processes are not rigorously established for a locally strained surface. Recent surface science modeling suggests adsorption control of da/dN based on similar dependencies of H₂O surface coverage and H-permeation on crack tip water vapor pressure^[82], both of which saturate (plateau) at values consistent with isolated literature $(P_{\text{H}_2\text{O}}/f)_{\text{sat}}$.^[49] However, the study did not address the $P_{\text{H}_2\text{O}}$ difference at the crack tip and crack mouth, the local strain (defect) dependence of reaction, the impact of H diffusivity, the influence of T , and reported data that do not plateau above $(P_{\text{H}_2\text{O}}/f)_{\text{sat}}$.^[34] The adsorption control contention is limited by these shortcomings and the lack of a quantitative model for da/dN . Speculatively, high crack tip strains and surface defects produced by cyclic plasticity strongly promote surface coverage of H₂O, H production rate, and H ingress into the lattice.^[83] This suggests that temperature induced reduction in reaction rate given by the Arrhenius model in Eq. [2] is of secondary importance.

Diffusion of surface absorbed H into the crack tip process zone to produce a critical H concentration for crack advance can be a rate-limiting factor, as

established for fatigue in 7000-series Al alloys under full immersion electrolyte conditions at 296 K (23 °C).^[77] For water vapor environments, Wei *et al.* proposed that when both water vapor transport and surface reaction are rapid, crack growth is rate limited by H diffusion^[51,84]:

$$\left(\frac{da}{dN}\right)_{cf} = A_O \left[\frac{P_{H_2O} D_H}{f}\right]^{\frac{1}{2}} \Delta K^2 \quad [3]$$

$$D_H = D_{H_0} \exp\left[\frac{-E_H}{RT}\right]$$

where A_O is an empirical constant, P_{H_2O} is crack mouth water vapor pressure, D_H is the trap sensitive effective diffusivity of H through the microstructure, D_{H_0} is the frequency factor, f is cyclic loading frequency and E_H is the activation energy for diffusion. Braun reported diffusivity values for H in 7075-T6 at 293 K (20 °C),^[85] the mean being $D_H = 3.7 \times 10^{-11} \text{ m}^2/\text{s}$.[§] With the standard

[§]This is a likely upper bound on D_H . Reported values are highly variable, with a range from $10^{-11} \text{ m}^2/\text{s}$ to $10^{-13} \text{ m}^2/\text{s}$ attributed to surface effects, low solubility of H, and hydrogen-microstructure trapping interaction.^[86-90]

Arrhenius relationship for the temperature dependence of D_H , and using material constants reported for a similar alloy, 7050, ($D_{H_0} = 2.2 \times 10^{-9} \text{ m}^2/\text{s}$, $E_H = 16.1 \text{ kJ/mol}$ ^[86]), decreasing temperature from 296 K (23 °C) will reduce D_H by 9 times at 223 K (−50 °C) and 60-fold at 183 K (−90 °C).^{§§} From Eq. [3],

^{§§}Braun did not report D_0 and E_H values for 7075-T6,^[85] as such the relative T dependence is estimated using 7050 data.

da/dN should be reduced by the square root of these diffusivity reductions multiplied by the reduction in P_{H_2O}/f above ice. The net effect of these temperature dependent terms is a 90-times reduction in da/dN for temperature decreasing from 296 K to 223 K (23 °C to −50 °C) and an additional 60-times reduction in da/dN for temperature decreasing from 223 K to 183 K (−50 °C to −90 °C). Directionally, the combined effect of decreasing H concentration (given by reduced P_{H_2O}/f) and decreasing H diffusivity is consistent with the temperature dependent reductions in da/dN . However, the model in Eq. [3] is not quantitatively consistent with the measurements shown in Figure 3. Specifically, the predicted 90-times then 60-times reductions in da/dN going from 296 K to 223 K to 183 K (23 °C to −50 °C to −90 °C) are not well aligned with $C-T$ results at ΔK of 5 MPa $\sqrt{\text{m}}$ that show a 36-fold reduction in measured da/dN from 296 K to 223 K (23 °C to −50 °C), followed by no additional da/dN reduction from 223 K to 183 K (−50 °C to −90 °C) (Figure 3). For the pit specimens represented in Table III, these measured-mean da/dN reductions are 34 times for chilling to 223 K (−50 °C) and an additional 6 times from 223 K to 183 K (−50 °C to −90 °C) (at ΔK of 3.0 MPa $\sqrt{\text{m}}$ where the analysis in

Section IV-B establishes that H uptake from precorrosion does not affect da/dN). This quantitative discrepancy is not surprising because the model represented in Eq. [3] assumes per-cycle crack growth and does not contain an explicit failure criterion detailing the critical H concentration necessary for crack advance.^[77] An improved H-diffusion model of da/dN is necessary.

The semi-quantitative comparison of measured da/dN vs temperature with the predictions of the Knudsen flow limited cracking model (Eq. [1]) and process zone H diffusion model (Eq. [3]) demonstrates the conditions where each capture the interactive effects of water vapor pressure, loading frequency, and H diffusivity on temperature dependent FCG. This suggests that modeling MSC da/dN using P_{H_2O-ICE} as a quantitative descriptor of the low temperature environment is not sufficient; the interaction of H diffusion and P_{H_2O}/f must be included. Figure 9 supports this conclusion by illustrating the moderate quality of the correlation between low temperature corrosion pit MSC (●) and vacuum-system controlled (■, ◇) results on a plot of da/dN vs P_{H_2O}/f . Also included are marker-band data (△) initiated from constituent particles at $R = 0.5$ and T of 296 K and 223 K (23 °C and −50 °C) ($f = 5$ and 10 Hz, respectively), as detailed elsewhere.^[91] Excellent agreement is observed for the $C-T$ and MSC data at the highest exposure condition restricted to 296 K (23 °C), as well as for the single pristine MSC data point at 223 K (−50 °C) and 0.32 Pa s. The comparable MSC pit result is at 223 K (−50 °C) and 0.13 Pa s is well below the 296 K (23 °C) exposure-based trend line. The P_{H_2O-ICE}/f for the 183 K (−90 °C) MSC pit experiment falls in the lower portion of the Knudsen flow regime at 3×10^{-4} Pa s, while the experiments at 223 K (−50 °C) and 296 K (23 °C) are characterized by exposure levels above $(P_{H_2O}/f)_{sat}$, 0.13 and 80 Pa s respectively, and well within the H diffusion controlled regime. At this ΔK a simple P_{H_2O-ICE}/f proxy for temperature will only effectively describe da/dN for exposure levels below $(P_{H_2O}/f)_{sat}$ (0.01 Pa s for 7075-T651). To guide broader consideration of temperature-dependent da/dN , literature results provide saturation pressures and growth rate data for: 7075-T651 at ΔK of 7 MPa $\sqrt{\text{m}}$ and R of 0.1,^[77] Al-Cu-Mg at ΔK of 7 MPa $\sqrt{\text{m}}$ and R of 0.6,^[47] and Al-Cu-Li at ΔK of 7 MPa $\sqrt{\text{m}}$ and R of 0.6.^[47] Values of $(P_{H_2O}/f)_{sat}$ and da/dN_{cf-sat} below which Knudsen flow is dominant are $3.6 \times 10^{-5} \text{ mm/cycle}$ and 0.8 Pa s, $3.2 \times 10^{-5} \text{ mm/cycle}$, and 0.2 Pa s, and $2.0 \times 10^{-5} \text{ mm/cycle}$ and 0.5 Pa s, respectively. In this regime P_{H_2O}/f may provide a simple proxy to describe temperature dependent da/dN for prognosis.

B. Mechanistic Interpretations of Fracture Morphology: Role of H

The fracture surface morphology is critical to understanding the active fatigue cracking mechanism, particularly the role of H from precorrosion as well as crack tip reaction with water vapor during cyclic deformation. Fractographic evidence suggests that the reduced growth rates at low temperatures (Figure 3) correlate with a change in fracture surface morphology (Figures 5, 6, 7). The flat facet-like features (~10 μm

wide) observed at crack depths of 200 to 1,500 μm in cold controlled pit tests and sparsely in cold EXCO at $\approx 500 \mu\text{m}$ are indicative of crack advance by localized-intense slip along crystallographic planes.^[45] This type of feature (Figure 7(c)) contrasts with those produced when the moist environment enhances da/dN ; for example, Figure 5. Similar slip band-like features were observed on C - T crack surfaces produced at low ΔK (2 to 4 $\text{MPa}\sqrt{\text{m}}$) in ultra-high vacuum at 296 K (23 $^\circ\text{C}$).^[67] This SBC mechanism is promoted by a lower stress intensity range that favors planar slip confined to deformation bands, and is active in the absence of a hydrogen influence.^[46,78] Lin *et al.* demonstrated that the strengthening precipitates in 7000-series alloys are shearable at a Cu content below ~ 1.6 wt pct; as such, SBC is reasonable even in this peak aged 7075-T651 with 1.66 wt pct Cu.^[68,69] These results confirm the hypothesis that da/dN decreases with decreasing temperature due to a reduction in the deleterious interaction of H with plasticity damage.

Understanding the origin of the non-SBC regions proximate to crack formation sites is not straight forward. The controlled pit 296 K (23 $^\circ\text{C}$) case (Figures 5(c) and 11(a)), and EXCO 223 K (-50°C) regions (Figures 8(b) and 11(e)), illustrate surfaces in the near-formation region that are flat and featureless on both the 10 to 80 μm and 0.1 to 1 μm size scales. Such morphologies are characteristic of H embrittlement. At 296 K (23 $^\circ\text{C}$), the moist-fatigue environment readily supplies the necessary H to the process zone. The peculiar flat features with fine-roughness (Figures 6(c), (d), 7(d), 11(b) and (c)) are present over the same depth ($\sim 250 \mu\text{m}$) for both 223 K and 183 K (-50°C and -90°C) controlled pit specimens, but only sporadically appear on the EXCO surface (Figure 11(d)) with no definitive transition to slip band cracking (Figure 8). A reasonable hypothesis is that the fine-roughness is also indicative of H-assisted cracking, but where the mechanical influence is higher than encountered for the more aggressive $P_{\text{H}_2\text{O}}/f$ situation at 296 K (23 $^\circ\text{C}$). Specifically, cracking progresses along dislocation cell boundaries formed from accumulated cyclic plasticity,^[46] but the low levels of H necessitate higher levels of plasticity accumulation for crack advance, causing a rougher fracture path along the cell interfaces. A purely mechanical origin for this crack morphology is discounted since this region transitioned to more faceted SBC with increasing crack depth away from the pit.

Two findings indicate that near-pit/EXCO cracking at each temperature is enhanced by H which must be dissolved in the microstructure prior to fatigue loading: (1) the absence of an external environment influence on da/dN at 223 K and 183 K (-50°C and -90°C), established by the C - T results in Figure 3, and (2) the lack of similar complex crack surface features adjacent to crack nucleating constituent particles for the non-precorroded fatigue case.^[91] Dissolved H likely results from corrosion,^[87,92–94] and precharged H promotes brittle fracture for monotonic loading.^[81,95,96] Assuming that movement of the pit front during corrosion is analogous to a propagating crack diffusion boundary

condition, the H concentration (C_{H}) gradient (normalized by the surface concentration, C_{HS}) is given by^[97]:

$$\frac{C_{\text{H}}}{C_{\text{HS}}} = \text{erfc} \left\{ \left(\frac{V}{2D_{\text{H}}} \right)^{0.5} (2x)^{0.5} \right\} \quad [4]$$

where x is the distance ahead of the perimeter of the pit, V is the corrosion front velocity estimated by dividing final pit depth by corrosion time, and D_{H} is defined in Eq. [3]. With a trap sensitive D_{H} , C_{H} includes mobile lattice H plus mobile-reversibly trapped H present at various microstructure features.^[87] Normalized H concentration profiles are plotted in Figure 12 for the controlled pit and EXCO exposures using $D_{\text{H}} = 3.7 \times 10^{-11} \text{ m}^2/\text{s}$ (bold line) and (± 50 pct of D_{H} (dotted lines). For assumed $D_{\text{H}} = 3.7 \times 10^{-11} \text{ m}^2/\text{s}$, there is significant H uptake ($C_{\text{H}}/C_{\text{HS}} > 0.2$) extending to a depth of $\approx 150 \mu\text{m}$ for pitting at 296 K (23 $^\circ\text{C}$). This distance, including the uncertainty due to D_{H} (see footnote 5) is similar to the distances shown in Figures 6 and 7, where the near-pit H cracking features transition to SBC at a depth of about 200 to 250 μm . The hydrogen penetration depths for EXCO exposures are deeper, consistent with the lack of SBC observed on the fracture surface in Figure 8. Comparison of controlled pit and EXCO results suggests similar C_{HS} . This correspondence with fracture surface characteristics is encouraging, but there are three complicating issues: (1) a high vacancy concentration within $\sim 1 \mu\text{m}$ of the corrosion front may inhibit H diffusion, (2) corroded specimens were stored for 1 to 2 weeks at 296 K (23 $^\circ\text{C}$) before fatigue testing, allowing time for H egress or homogenization within the specimen, and (3) the critical concentration to cause H assisted fatigue is not defined. These complications are considered.

First, both H and vacancies are injected into Al about the perimeter of the acidified-dissolving corrosion pit.^[87] It is energetically favorable for H and vacancies to combine, forming a $\sim 1 \mu\text{m}$ region highly concentrated with H-vacancy complexes (Figure 13).^[93,98,99] The high H-vacancy binding energy ($E_{\text{HV}} \sim 50 \text{ kJ/mol}$) causes very low effective diffusivity of H in Al in the presence of vacancies[†]

[†]The ratio of H lattice concentration ($C_{\text{H-L}}$) to the concentration of H-vacancy complexes ($C_{\text{H-V}}$) is directly proportional to the ratio of effective H diffusivity in the presence of vacancies ($D_{\text{H-eff}}$) to H diffusivity in the Al lattice slowed by reversible microstructure trapping (D_{H}). Taking the relationship $C_{\text{H-V}} = C_{\text{H-L}} \exp[E_{\text{HV}}/RT]$,^[100] it is possible to estimate the vacancy-reduced diffusivity as $D_{\text{H-eff}} = D_{\text{H}}/\exp[E_{\text{HV}}/RT]$.

($D_{\text{H-eff}} = 5 \times 10^{-20} \text{ m}^2/\text{s}$) consistent with H-trapping considerations.^[86,92,101] Also important is the diffusivity of the combined H-vacancy complex ($D_{\text{H-V}}$) in Al which Buckley reported as faster ($4 \times 10^{-15} \text{ m}^2/\text{s}$),^[99] but still slow relative to the intrinsic lattice and reversible-trap sensitive D_{H} of $4 \times 10^{-11} \text{ m}^2/\text{s}$. For these reduced $D_{\text{H-V}}$ ($4 \times 10^{-15} \text{ m}^2/\text{s}$) and $D_{\text{H-eff}}$ ($5 \times 10^{-20} \text{ m}^2/\text{s}$), the calculated H or H-vacancy complex penetration during pre-corrosion exposure falls below $1 \mu\text{m}$; substantially less than the concentration profiles shown in Figure 12. A countering

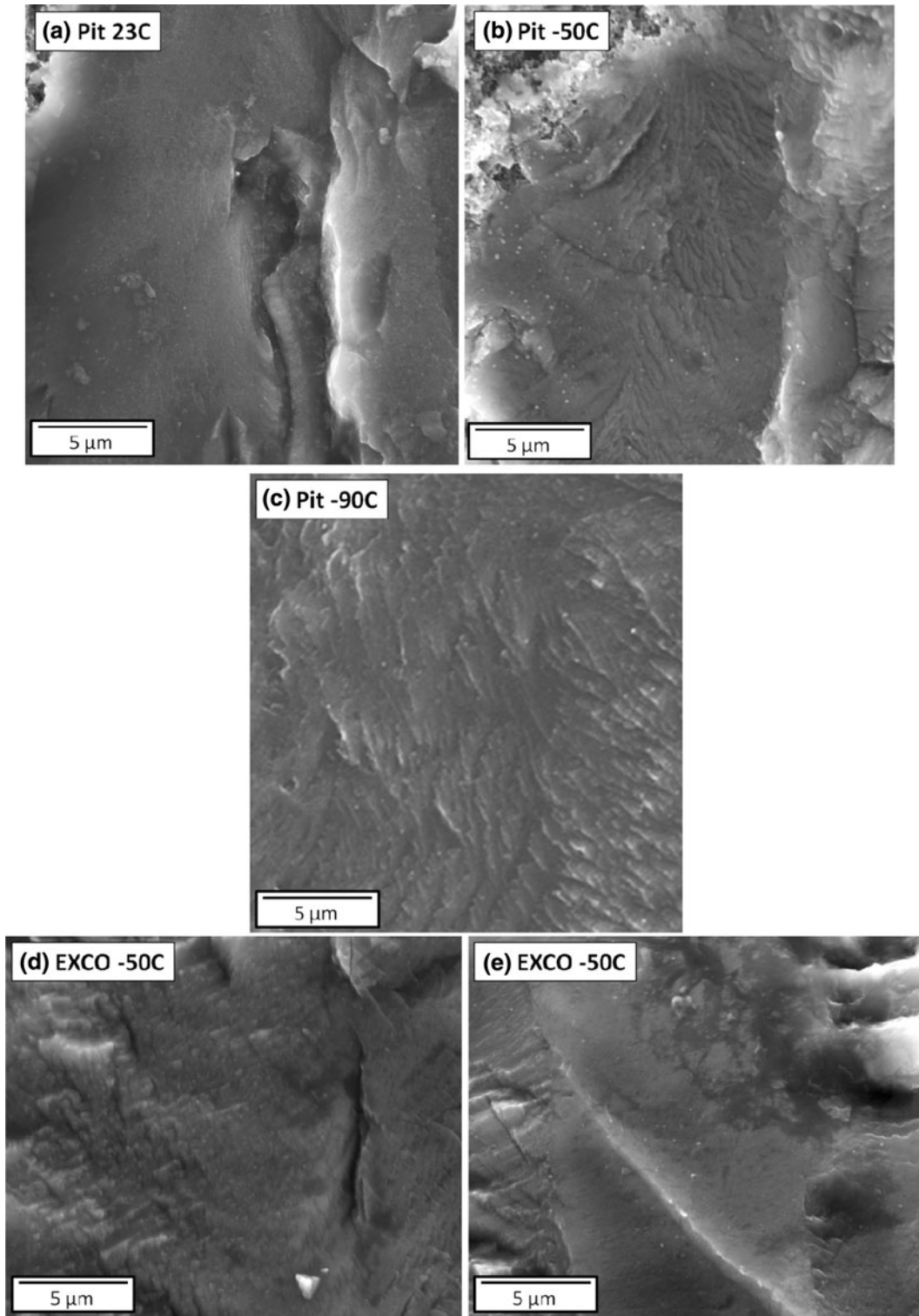


Fig. 11—High-magnification fractographs of the *T-S* fracture plane of 7075-T651 pit (*a* to *c*) and EXCO corroded (*d*, *e*) fatigue specimens tested in: (a) water saturated N_2 at 296 K (23°C), (b, d, e) dry N_2 at 223 K (−50°C), and (c) dry N_2 at 183 K (−90°C). Each image was taken within 20 μm of the formation site; (a) and (e) distinguish the flat smooth morphology from the flat fine-roughness morphology in (b to d).

increase in H mobility could be facilitated by two mechanisms. First, if the rate of H injection greatly exceeds that of vacancies, then vacancy sites become saturated allowing $D_{\text{H-eff}}$ to approach the level not affected by vacancy

trapping. This requires an abundance of H since a single vacancy traps up to 12 H atoms.^[102] Secondly, when large concentrations of H-vacancy pairs are present, aggregation produces voids (Figure 13),^[98,102] within which H either

recombines to form H₂ (significant H absorption would not be expected from such a molecular gas environment^[82,87,103]) or the atomic H is absorbed. The lack of oxide within voids facilitates the latter producing interstitial H, which would presumably diffuse at the lattice/reversible-trap sensitive diffusivity of H in 7075-T651. Either of these events must occur in order for the

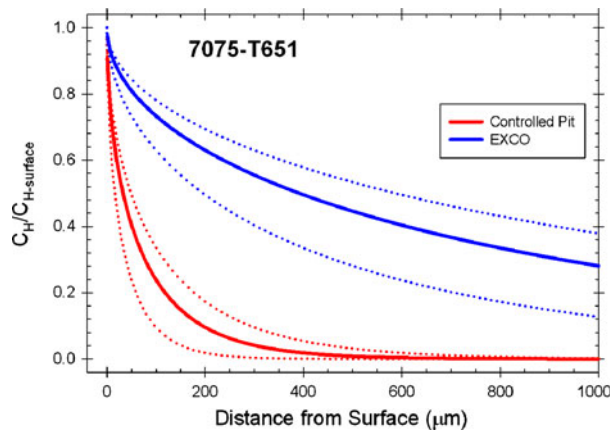


Fig. 12—The concentration of H dissolved in 7075-T651, normalized by the surface concentration from corrosion, vs distance from the H-charging surface. Concentration is calculated assuming a moving front diffusion solution^[97] applied to the controlled pit and EXCO exposure cases where $3.7 \times 10^{-11} \text{ m}^2/\text{s}$ (bold-lines) is the assumed D_H and dotted lines represent ± 50 pct variations in H diffusivity (Color figure online).

penetration profiles in Figure 12 to provide a reasonable explanation of the observed fractographic features about corrosion pits.

As a second complication, between corrosion and fatigue stressing (1 to 2 weeks), the specimen was stored in a desiccator at room temperature where H-egress or homogenization could occur. The oxide layer on the pit/specimen surface would likely retard H escape to the external environment. Homogenization into the specimen may be mitigated by the substantial increase in the bulk vacancy concentration (C_V) stabilized by H according to the following relationship^[92]:

$$C_V = \exp\left(\frac{-[H_v^f - E_{HV}]}{RT}\right) \quad [5]$$

where the vacancy formation enthalpy (H_v^f) is 63.5 kJ/mol for Al^[104] and is decreased by the binding energy of the H-vacancy trap site ($E_{HV} \sim 50$ kJ/mol).^[86,92,101] From Eq. [5], vacancy concentration increases from 6×10^{-12} to 4×10^{-3} vacancies per lattice site in the presence of H. The newly formed-stabilized vacancies serve as H trap sites, throughout the hydrogenated region represented in Figure 13, which could lock the H concentration gradient at post corrosion levels. The unknown kinetics of vacancy formation and H-vacancy coupling, relative to H diffusivity, complicate this speculation. Vacancy formation occurring slower than H diffusion in Al would allow homogenization of H into the material, thus diluting the concentration gradient compared to the

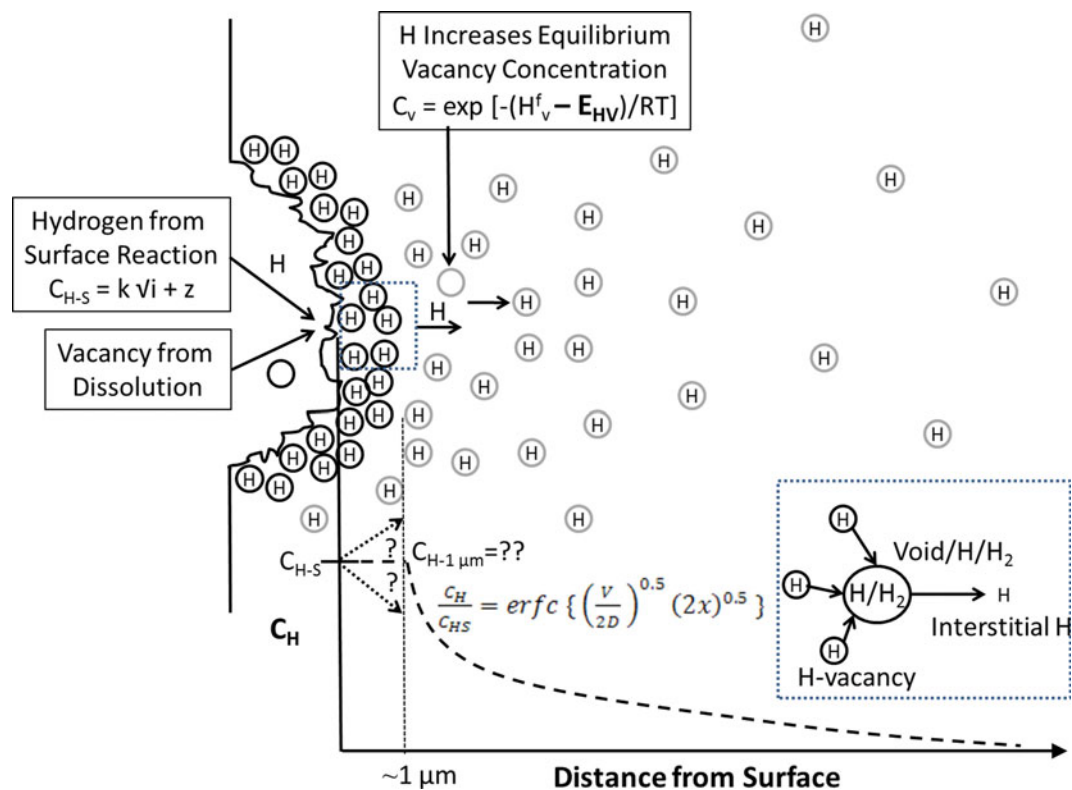


Fig. 13—H charging and vacancy injection during pit corrosion. The dashed box illustrates combination of H-vacancy complexes to form 100 nm voids containing atomic H and H₂, where absorption into interstitial sites allows the H to diffuse into the material.

estimates in Figure 12. Conversely, if vacancy formation is rapid compared to H diffusion, then vacancy trapping would localize H about the pit. Fractographic evidence (Figures 6 and 7) suggests that a H-vacancy gradient similar to Figure 12 is stabilized in the material. During room-temperature storage, the H-vacancy complex could homogenize; using $D_{H-V} = 4 \times 10^{-15} \text{ m}^2/\text{s}$, H diffuses $\sim 100 \text{ }\mu\text{m}$ in 14 days. Such variation in the Figure 12 gradient would not detract from the reasonable agreement between the observed length scale of the flat fracture surface regions in Figures 6 and 7.

As a third complication, the lack of a quantitative failure criterion to establish the critical level of H concentration, plastic damage accumulation, and tensile stress necessary for fatigue crack formation and advance precludes quantitative assessment of cracking. Regardless, it is useful to estimate H concentrations to determine if the pre-charged H levels could contribute to fatigue. The relationship $C_{HS} = k\sqrt{i} + z$ is used to estimate C_{HS} (Figure 13), where i is assumed to equal 50 pct of the galvanostatic current used to produce a pit.^[105] The empirical constants (k and z) are not available for 7075, but values reported for a Ni-Cu alloy (Monel K-500) are justified by similarities observed for a range of FCC alloys.^[106] The resulting estimate of C_{HS} is $\sim 5,000$ ppmw and a Faradaic analysis suggests that the EXCO values will be on the same order. If Figure 12 accurately represents the H concentration distribution, then the fracture surface change at ~ 150 to $200 \text{ }\mu\text{m}$ from flat with fine-roughness to slip-band like morphology suggests that ~ 10 to 20 pct of the controlled pit C_{HS} ($C_H \approx 500$ to 1000 ppmw) represents a threshold internal H content for enhanced cracking at this ΔK and f .

Despite the uncertainties associated with H and vacancy uptake, diffusion during the corrosion process, and homogenization during storage; the speculation that the ~ 150 to $250 \text{ }\mu\text{m}$ fine-roughness regions are due to low level H embrittlement coupled with high levels of accumulated plasticity is reasonable. Furthermore, it is reasonable to assume H concentration gradients similar to those in Figure 12 in order to analyze crack formation and growth measurements.

C. Crack Formation

Fatigue crack formation occurs when the accumulated plasticity due to the local plastic strain range exceeds the material resistance threshold. Material resistance can be degraded within this process zone by embrittlement involving interaction of the local H concentration (see Figures 12 and 13) with the micro-scale tensile and hydrostatic stress distributions. The dramatic increase in corroded specimen N_i from humid 296 K (23 °C) stressing (35,000 cycles, Table I) to fatigue at 223 K (−50 °C) (1,291,000 cycles) and 183 K (−90 °C) (4,345,000 cycles) is first explained by the notion that the concentration of H achieved by water vapor reaction during cyclic stressing decreases as temperature decreases the P_{H_2O} . However, the fracture surface features [similar for 183 K and 223 K (−90 °C and −50 °C)] suggest that H participates in fatigue damage even at 183 K (−90 °C), where very low P_{H_2O}

likely preclude environmental embrittlement. This suggests an increased role of precharged H as temperature falls. Furthermore, the variation in N_i between 223 K and 183 K (−50 °C and −90 °C) suggests an influence of: (1) residual-environment reaction at −50 °C due to a very short ($< 20 \text{ }\mu\text{m}$) Knudsen flow distance from the crack tip to the external environment, (2) time-temperature dependent H diffusion, and/or (3) temperature dependence of per cycle stress, strain, and dislocation evolutions.^[78] Neither (1) nor (3) explain the transition from H-assisted to SBC at nearly identical depths for the two different external P_{H_2O-ICE}/f values at 223 K and 183 K (−50 °C and −90 °C).

The precharged H-vacancy concentration gradients are formed by controlled pit and EXCO corrosion exposures at 296 K (23 °C) (Figure 12) and as such are initially independent of loading temperature. However, the variation between N_i from 223 K to 183 K (−50 °C to −90 °C) could be attributed to a decrease in diffusivity of precharged H or H-vacancy complexes with decreasing temperature, this would slow transport to the formation site during cyclic stressing. This is consistent with lower EXCO N_i relative to controlled pits at lower temperatures (Table I). Figure 12 suggests more internal H-vacancy complexes in EXCO specimens, so it is reasonable to assume that the critical H concentration would be achieved in fewer load cycles than for controlled pits. Formation life variation due to temperature dependent diffusion is reasonable and correlates with the experimental data; however, this speculation depends on either dissociation of the H-vacancy complex allowing for H diffusion,^[107–109] or a driving force for diffusion of a H-vacancy complex towards a high stress and plastic strain formation site.

The driving forces for H redistribution by diffusion to the crack formation site are the gradients of local plastic strain (ϵ_p), and hydrostatic stress (σ_{HS})^[107–109]; both of which are high near the pit perimeter fatigue crack forma-

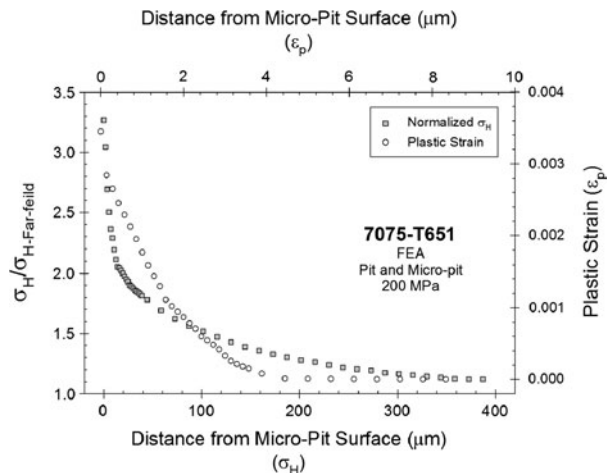


Fig. 14—Hydrostatic stress (normalized by the far-field hydrostatic stress), as well as plastic strain, about a $232 \text{ }\mu\text{m} \times 624 \text{ }\mu\text{m}$ corrosion pit containing a micro-pit of $15 \text{ }\mu\text{m}$ diameter vs distance from the micro-pit surface. The values were obtained by monotonic elastic-plastic FEA analysis at an applied stress of 200 MPa, as detailed in Ref. [52].

tion site (Figure 14). The H-vacancy binding energy ($E_{HV} \sim 50$ kJ/mol) is well above the binding energy between H and dislocations ($E_{HD} \sim 30$ kJ/mol).^[86] However, cyclic loading produces an abundance of dislocations that arrange into complex cells and subgrain structures in Al alloys.^[46] In the limit these dislocation structures could arrange to form nano-scale vacancies or voids intermingled with complex dislocation cell wall structure.^[110] Recent simulations suggest that Al grain boundaries strongly trap H,^[111] consistent with findings for steel where H binding energies are ~ 60 kJ/mol^[100,112] and 90 kJ/mol^[100] for standard and highly misoriented grains, respectively. Cyclic damage may evolve a dislocation structure such that binding energy increases from ~ 30 kJ/mol to levels analogous to H trapping at vacancies, grain boundaries, or voids (~ 60 kJ/mol to 90 kJ/mol). The probability that H occupies the cyclic damage structure (P_{H-D}) vs occupation of H-vacancy complex is given by^[100,113]:

$$P_{H-D} = \frac{\exp\left[\frac{E_{HD}}{RT}\right]}{\exp\left[\frac{E_{HD}}{RT}\right] + \exp\left[\frac{E_{HV}}{RT}\right]} \quad [6]$$

where $E_{HV} \sim 50$ kJ/mol^[86,92,101] and E_{HD} is damage structure binding energy. For 223 K (-50 °C), assuming E_{HD} of 30, 45 and 60 kJ/mol, the P_{H-D} are 2×10^{-5} , 0.06, and 0.99, respectively, and 183 K (-90 °C) values are similar. As the cyclic damage evolves, it is possible that the H-vacancy complex will dissociate and atomic H will diffuse to the high stress and strain sites within the pit-mechanical process zone. Reduced H mobility at 183 K (-90 °C) compared to 223 K (-50 °C) could explain the increased number of load cycles required for H-affected fatigue crack formation at the lower temperature.

If the H-vacancies do not dissociate, then the mechanism and origin of the driving force for transport of the H-vacancy complex are less straightforward. The H-vacancy diffusivity can be estimated ($D_{H-V} = 4 \times 10^{-15}$ m²/s) and likely exhibits an Arrhenius temperature dependence.^[86,99] Elastic dislocation theories in general suggest an attractive force between dislocations and vacancies,^[114,115] furthermore researchers have shown a stress field attractive interaction between H and dislocations.^[37] However, the attractive force between H-vacancy complexes and dislocations or hydrostatic stresses has not been studied. Despite the uncertainty associated with the mechanism for H-vacancy dissociation and/or H-vacancy transport, the fractography and N_i measurements suggest a driving force for the temperature dependent diffusion of internal H to the high hydrostatic stress/plastic strain crack formation site even at 183 K (-90 °C). Research is required to establish the details of this time-temperature dependent redistribution of H.

D. Crack Propagation

1. Role of H source

Experimental results establish that low temperature stressing environments decrease MSC growth rates for both the pit and EXCO specimens (Figures 3, 4 and Table III). These findings are consistent with alloy

2024 long crack data gathered at 223 K (-50 °C) in ambient air and 223 K (-50 °C) vacuum (10^{-4} Pa),^[116,117] where the cold specimens exhibited vacuum-like da/dN levels and a slip-band fracture surface morphology. Interpretation of the MSC propagation data varies with temperature and crack depth relative to the depth of corrosion-H penetration developed in Section IV-B. Stressing in moist N₂ at 296 K (23 °C) produces sufficiently high levels of crack tip P_{H_2O} and C_{HS} , coupled with rapid reaction and diffusion kinetics, to marginalize the effect of H pre-charged during corrosion. This interpretation is consistent with the similarity between EXCO, controlled pit, and pristine crack growth rate results (see Figures 4 and 9, and Reference 91).

Interpretation of the MSC growth rates at 223 K and 183 K (-50 °C and -90 °C) requires recognition of the dominant H source. The fractographic results, H diffusion analysis, and speculative H-vacancy trapping scenario (Section IV-B and Figure 13) establish that H from corrosion affects MSC over a distance up to 200 to 250 μ m beyond the pit perimeter (Figures 6 through 13). The depth of H-affected MSC was much larger for EXCO specimens. Considering the pit specimens, a depth of 200 to 250 μ m corresponds to a ΔK of 2.4 to 2.6 MPa \sqrt{m} ; MSC data should only be directly comparable to long crack $C-T$ specimen data for ΔK above this level. Figure 3 qualitatively confirms this hypothesis, at ΔK below about 2 MPa \sqrt{m} , MSC rates systematically exceed da/dN values suggested by extrapolations of the $C-T$ data for 223 K and 183 K (-50 °C and -90 °C).^{¶¶}

^{¶¶}Newman suggested that the apparent long crack threshold shown for the $C-T$ data in Figure 3 is a crack wake plasticity/closure artifact of $C-T$ testing^[118-120]; as such the pre-threshold growth regimes are often extrapolated to lower ΔK as illustrated by the dotted lines.^[11,12,23,24] Complications with such extrapolation are discussed elsewhere.^[23]

Moreover, the limited ΔK levels above this corrosion-H affected regime show a dip or plateau in MSC growth rates. This behavior corresponds with the onset of slip-band like fracture surface features (Figures 6 and 7), which suggests a lack of H assisted cracking beyond the precharged H region. The MSC rates for EXCO precorrosion may not be directly comparable to the $C-T$ data at any ΔK examined due to the deeper penetration of pre-charged H into the material (Figure 12). This view is supported by Figure 4 (particularly 223 K (-50 °C) data) where EXCO data agree well with the corrosion-H affected portion of the pit data, exceed long crack $C-T$ data extrapolations, and do not show the decrease from power law behavior in the 200-250 μ m (2.4 to 2.6 MPa \sqrt{m}) regime. Furthermore, Figures 8(a) and (c) show no definitive transition to SBC for EXCO specimens.

While there is significant overlap in the 223 K and 183 K (-50 °C and -90 °C) MSC rate data (Table III), on-average there is a ≈ 2 to 3-fold decrease in growth rates at 183 K (-90 °C). This is likely due to temperature dependent diffusion of precharged H

(or H-vacancy complexes) to the crack tip (Section 4.2). This hypothesis is qualitatively consistent with the similar flat fine-roughness morphology depths for 223 K and 183 K (−50 °C and −90 °C) (Figures 6 and 7) and the dip/leveling (Figure 3) of the cold data at 2 MPa√m where the precharged H concentration is no longer sufficient to embrittle the material. Despite the scarcity of the marker-band da/dN data above 2 MPa√m and 150 μm, the persistent variation (Table III) between the 223 K and 183 K (−50 °C and −90 °C) results is troublesome since such behavior is not observed in the C - T data. Possible influences of temperature dependent cyclic plastic damage accumulation (specifically dislocation mobility^[75,78]), or a lingering environmental contribution at small crack lengths (<500 μm) and low crack wake Knudsen transport distances may cause this discrepancy. The latter is not likely since the observed SBC is not expected for even marginally H-enhanced crack growth.^[34]

2. Impact on fatigue prognosis

The MSC growth rate data presented in Figures 3 and 4, summarized in Table III, provide the first quantitative results to enable prognosis of fatigue life at cold temperatures. The use of such data in fatigue prognosis was discussed for MSC in 7075-T651 stressed at 296 K (23 °C).^[23,24] Issues unique to cold temperatures are highlighted here.

a. Stress intensity range. Consistent with 296 K (23 °C) results,^[23] Figures 3 and 4 illustrate that stress intensity range reasonably correlates MSC growth rates, including cracking at ΔK levels between 0.2 and 1 MPa√m. These da/dN vs ΔK data, with statistics summarized in Table III, can be used in probabilistic models of component life. The discussion of the effect of corrosion-charged H should be considered when applying these results to corroded surfaces.

The large degree of variability observed in Figures 3 and 4 and presented in Table III reflects real crack front undulations captured by the high fidelity marker-banding technique and attributed to crack front interaction with microstructural features.^[23] As the environmental and precharged H influences decrease, the variability in da/dN at a given ΔK should increase, since the effects of grain-to-grain plasticity variation and crack front intersection with constituents and grain boundaries will not be dominated by embrittling H effects. This expectation is realized on average. At the ΔK levels analyzed in Table III, the data which reflect H-environment embrittlement at 296 K (23 °C) exhibit a weighted mean variability of ±99 pct (ranging from ±34 to 126 pct variation). Whereas the mean variability for cold controlled pit and EXCO data increases to ±166 pct (range ±54 to 378 pct) and 121 pct (range ±22 to 132 pct), for 223 K and 183 K (−50 °C and −90 °C), respectively. The high 223 K (−50 °C) value reflects the high calculated variability for the controlled pit at $\Delta K = 3$ MPa√m (±378 pct) due to the staggered onset of the growth rate dip/plateau associated with elimination of the corrosion-H effect. If this variability is excluded,

then the mean value for 223 K (−50 °C) (±120 pct) aligns well with 183 K (−90 °C) variability (±121 pct). Analysis of the cold data in Table III shows that the variability scales with the expected level of corrosion precharged H (Figure 12). Specifically, the mean variability over the four stress levels is lower for highly H-charged EXCO (±59 pct at 223 K (−50 °C) and ±47 pct at 183 K (−90 °C)) compared to mean controlled pit values (±158 pct at 223 K (−50 °C) and ±116 pct at 183 K (−90 °C)).

b. Cyclic crack tip opening displacement. Crack tip opening displacement (ϕ) provides an alternate approach to modeling the driving force for fatigue crack growth and is mechanically satisfying due its direct relationship with crack tip strain. Previous work^[23] established that cyclic crack tip displacement correlated 296 K (23 °C) marker-band data from different stress levels and controlled pit shapes, according to $da/dN \sim \alpha^2 \phi_c^{1.53}$ and better than competing theories.^[55,121] Figure 15 plots this relationship using temperature appropriate modulus and σ_{ys} . The ϕ_c is calculated using the Bilby, Cottrell and Swinden dislocation model for an elastic–plastic description of crack tip opening in the infinite center-cracked plate configuration.^[122] The α accounts for the effects of applied stress gradient and crack geometry, as estimated from elastic K , and is squared based on the continuum relationship, $\phi_c \sim \Delta K^2$.^[76] Full details of this calculation are given elsewhere.^[23] The MSC rate data are reasonably collapsed at each temperature, with scatter that is qualitatively similar to that observed in Figures 3 and 4. However, the failure of this plasticity-based method to collapse data from separate temperatures reaffirms the importance of loading environment, precharged H, and to a lesser extent temperature dependent plasticity; as previously discussed. A mechanically informed model must couple an accurate description of the local plasticity and environment with appropriate failure criteria for crack advance.

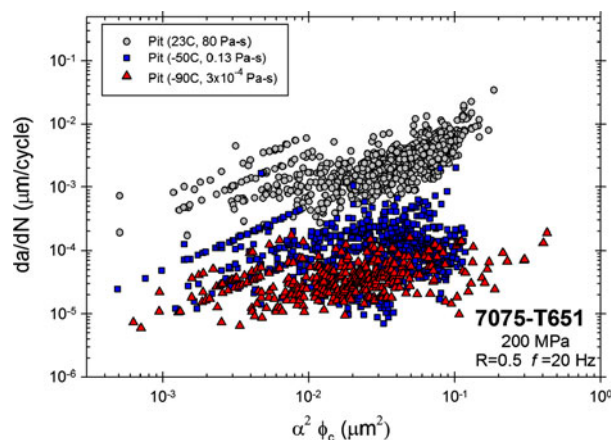


Fig. 15—Fatigue crack growth rate vs a dislocation based cyclic crack tip opening displacement parameter. The da/dN data are gathered from marker-band analyses of 7075-T651 controlled pit specimens, tested at $\sigma_{max} = 200$ MPa and $R = 0.5$ in water saturated N_2 at 296 K (23 °C), and in nominally dry N_2 at 223 K and 183 K (−50 °C and −90 °C) (Color figure online).

c. Application. The current work quantifies and provides a mechanistic foundation for the strong effect of temperature on the formation and MSC behavior of fatigue cracks about corrosion damage in 7075-T651. Companion work^[29] couples previously developed life prediction capabilities^[12,24,52] with this to demonstrate the feasibility of reducing conservatism by modeling fatigue crack progression to 500 μm at low temperatures. Figure 3 shows that $P_{\text{H}_2\text{O}}$ alone does not fully describe fatigue behavior; however, the temperature-induced reduction in $P_{\text{H}_2\text{O}}$ significantly contributes to the reduced da/dN . As such, from an engineering perspective, scaling of da/dN by $(P_{\text{H}_2\text{O}}/f)$ will reduce part of the conservatism associated with sole reliance on a 296 K (23 °C) humid air database. Consideration of the level of $(P_{\text{H}_2\text{O}}/f)_{\text{sat}}$ will improve the accuracy of this approach. While this is a first step towards reducing the inspection burden,^[29] important deficiencies must be addressed prior to mechanism-based incorporation of temperature into structural health prognosis. Needed inputs include: better modeling of H-diffusion limited crack growth, development of the time-cycle dependence of the H-damage mechanism put forth above, identifying a coupled in-flight environment-loading spectrum which accounts for meteorological variations with altitude and prior ice formation, and incorporating this understanding into an engineering level model that accounts for the coupled mechanical and environmental contributions in prediction of remaining component life.

V. CONCLUSIONS

Analysis of fatigue crack surface marker-bands on 7075-T651 individual-controlled pit and EXCO corroded specimens tested in ambient temperature humid and low temperature dry environments yields quantitative fatigue crack formation and microstructure scale crack (MSC) propagation data. These results impact fatigue life prediction, and are coupled with fracture surface morphology analyses and variable environment long crack C - T growth rates to establish likely mechanisms responsible for temperature dependent fatigue behavior. The following conclusions are established.

1. A substantial fatigue crack formation and propagation database defines the effect of low temperature stressing environment on MSC fatigue cracking emanating from localized corrosion topography in a commercial Al-Zn-Mg-Cu alloy.
2. Crack growth rates correlate with either elastic stress intensity range or cyclic crack tip opening displacement, and are available to predict corrosion effects on airframe fatigue for the important low temperature regime.
3. Fatigue resistance increases by up to several orders of magnitude with decreasing temperature from 296 K to 183 K (23 °C to -90 °C), as quantified by crack formation life about pit and EXCO corrosion topographies, MSC growth rates in the size scale

from 20 to 500 μm beyond the corrosion front, and long crack growth rates.

4. Warm-moist environment fracture surface features and cracking kinetics are consistent with dominant hydrogen environment embrittlement (HEE), including flat-smooth facets proximate to the formation site with no evidence of slip band cracking. The fatigue crack surfaces of cold specimens are substantially different, reflecting embrittlement due to H from corrosion within 200 μm of the pit surface, transitioning to faceted slip band cracking characteristic of inert environment H-free fatigue.
5. Decreasing temperature to 223 K (-50 °C) eliminates HEE through reduced water vapor pressure in equilibrium with ice, interacting with reduced H diffusion kinetics. The Knudsen flow model and exposure parameter, $P_{\text{H}_2\text{O}}/f$, enables improved modeling of temperature dependent cracking, but may not fully describe low temperature fatigue behavior due to possible rate limitation by H diffusion.
6. Localized corrosion prior to fatigue develops a H (or H-vacancy complex) concentration gradient about the pit surface which promotes low temperature crack formation and MSC propagation rate over a depth of ~200 μm , but is overwhelmed by HEE in moist 296 K (23 °C) environments. Declining MSC da/dN from 223 K to 183 K (-50 °C to -90 °C) is likely caused by reduced mobility of corrosion-precharged H.

ACKNOWLEDGEMENTS

This research was sponsored by the United States Air Force Research Laboratory (AFRL), Materials and Manufacturing Directorate, and the University Corrosion Collaboration managed by the DoD Office of Corrosion Policy and Oversight. Drs. John Papazian (deceased) and Elias Anagnostou of Northrop-Grumman Corporation provided 7075-T651, as well as Northrop-Grumman Industry Liaison funding. Mr. Phil Blosser and Mark Ruddell assisted with fatigue experiments at AFRL, and Mr. Yongwon Lee and Dr. Jiahe Ai conducted vacuum system fatigue experiments at UVA with important inputs from Prof. Ralph Bush of the United States Air Force Academy. Dr. Ivan Coles (Commonwealth Scientific and Industrial Research Organisation) provided advice on high altitude environmental conditions. These contributions are gratefully acknowledged. The views and conclusions contained herein are those of the authors and should not be interpreted as necessarily representing the official policies and endorsements, either expressed or implied of US Air Force Academy or the US Government.

REFERENCES

1. J. Papazian, E.L. Anagnostou, R.J. Christ, S.J. Engel, D. Fridline, D. Hoitsma, J. Madsen, J. Nardiello, J. Payne, R.P. Silberstein, G. Welsh, and J.B. Whiteside: *HR0011-04-C-0003*, DARPA, Arlington, VA, 2009.
2. L. Molent: *Int. J. Fatig.*, 2010, vol. 32, pp. 639-49.

3. G.A. Shoales, S.A. Fawaz, and M.R. Walters: *ICAF 2009 - Bridging the Gap Between Theory and Operational Practice*, M. Bos, ed., Springer, Rotterdam, The Netherlands, 2009, pp. 187–207.
4. G.A. Shoales, S.R. Shah, J.W. Rausch, M.R. Walters, S.R. Arunachalam, and M.J. Hammond: USAFA-TR-2006-11, USAF, Robins AFB, GA, 2006.
5. G.H. Koch, E.L. Hagerdorn, and A.P. Berens: AFRL-VA-WP-TR-2004-3057, AFRL, Wright-Patterson AFB, OH, 1995.
6. G.K. Cole, G. Clark, and P.K. Sharp: DSTO-RR-0201, DSTO, Melbourne, Australia, 1997.
7. M.E. Hoffman and P.C. Hoffman: *Int. J. Fatig.*, 2001, vol. 23, pp. S1–10.
8. H. Weiland, J. Nardiello, S. Zaefferer, S. Cheong, J. Papazian, and D. Raabe: *Eng. Fract. Mech.*, 2009, vol. 76, pp. 709–14.
9. J.E. Bozek, J.D. Hochhalter, M.G. Veilleux, M. Liu, G. Heber, S.D. Sintay, A.D. Rollett, D.J. Littlewood, A.M. Maniatty, H. Weiland, R.J. Christ, J. Payne, G. Welsh, D.G. Harlow, P.A. Wawrzynek, and A.R. Ingraffea: *Model. Simul. Mater. Sci.*, 2008, vol. 16, pp. 1–28.
10. J.M. Emery, J.D. Hochhalter, P.A. Wawrzynek, G. Heber, and A.R. Ingraffea: *Eng. Fract. Mech.*, 2009, vol. 76, pp. 1500–30.
11. S. Kim, J.T. Burns, and R.P. Gangloff: *Eng. Fract. Mech.*, 2009, vol. 76, pp. 651–67.
12. J.T. Burns, S. Kim, and R.P. Gangloff: *Corros. Sci.*, 2010, vol. 52, pp. 498–508.
13. B.R. Crawford, C. Loader, A.R. Ward, C. Urbani, M.R. Bache, S.H. Spence, D.G. Hay, W.J. Evans, G. Clark, and A.J. Stonham: *Fatig. Fract. Eng. M.*, 2005, vol. 28, pp. 795–808.
14. E.A. DeBartolo and B.M. Hillberry: *Int. J. Fatig.*, 2001, vol. 23, pp. S79–S86.
15. D.L. DuQuesnay, P.R. Underhill, and H.J. Britt: *Int. J. Fatig.*, 2003, vol. 25, pp. 371–77.
16. K.M. Gruenberg, B.A. Craig, B.M. Hillberry, R.J. Bucci, and A.J. Hinkle: *Int. J. Fatig.*, 2004, vol. 26, pp. 615–27.
17. M. Liao, G. Renaud, and N.C. Bellinger: *Int. J. Fatig.*, 2007, vol. 29, pp. 677–86.
18. J.J. Medved, M. Breton, and P.E. Irving: *Int. J. Fatig.*, 2004, vol. 26, pp. 71–80.
19. K.K. Sankaran, R. Perez, and K.V. Jata: *Mater. Sci. Eng. A*, 2001, vol. 297, pp. 223–29.
20. K. Sharp, T. Mills, S. Russo, G. Clark, and Q. Liu: *FAA/DoD/NASA Aging Aircraft 2000*, St Louis, MO, 2001.
21. K. van der Walde, J.R. Brockenbrough, B.A. Craig, and B.M. Hillberry: *Int. J. Fatig.*, 2005, vol. 27, pp. 1509–18.
22. K. van der Walde and B.M. Hillberry: *Int. J. Fatig.*, 2007, vol. 29, pp. 1269–81.
23. J.T. Burns, J.M. Larsen, and R.P. Gangloff: *Int. J. Fatig.*, 2011, vol. 42, pp. 104–21.
24. J.T. Burns and R.P. Gangloff: *Proc. Eng.*, 2011, vol. 10, pp. 362–69.
25. J.B. de Jonge and D.J. Spiekhou: in *Service Fatigue Loads Monitoring, Simulation, and Analysis*, ASTM STP 671, P.R. Abelkis and J.M. Potter eds., ASTM International, West Conshohocken, PA, 1979, pp. 48–66.
26. R.J.H. Wanhill: *NRL-TP-2001-545*. NRL, Amsterdam, The Netherlands, 2001.
27. U.S. Committee on Extension of the Standard Atmosphere: NASA-TM-X-74335 (NOAA-S/T 76-1562), NASA/NOAA/USAF, Washington, D.C., 1976.
28. D.A. Skinn, J.P. Gallagher, A.P. Berens, P.D. Huber, and J. Smith: *WL-TR-94-0452*. AFRL/Materials Directorate, Wright-Patterson AFB, OH, 1994.
29. J.T. Burns, R.P. Gangloff, and R.W. Bush: *DoD/NACE Corrosion Conference*, Palm Springs, CA, 2011.
30. R.P. Gangloff: in *Fatigue 2002*, A. Blom, ed., EMAS, Stockholm, Sweden, 2002.
31. J. Petit, G. Henaff, and C. Sarrazin-Baudoux: in *Comprehensive Structural Integrity: Environmentally Assisted Fracture*, J. Petit and P. Scott eds., Elsevier, New York, NY, 2003, pp. 962–70.
32. R.P. Wei: *Fracture Mechanics: Integration of Mechanics, Materials Science, and Chemistry*, Cambridge University Press, Cambridge, 2010.
33. Y. Ro, S.R. Agnew, and R.P. Gangloff: *Metall. Mater. Trans. A*, 2008, vol. 39A, pp. 1449–65.
34. Y.J. Ro, S.R. Agnew, G.H. Bray, and R.P. Gangloff: *Mater. Sci. Eng. A*, 2007, vol. 468, pp. 88–97.
35. S.P. Lynch: *Corros. Sci.*, 1982, vol. 22, pp. 925–37.
36. R.A. Oriani: *Corrosion*, 1987, vol. 43, pp. 390–97.
37. I.M. Robertson: *Eng. Fract. Mech.*, 2001, vol. 68, pp. 671–92.
38. F. Menan and G. Henaff: *Mater. Sci. Eng. A*, 2009, vol. 519, pp. 70–76.
39. Y. Murakami and S. Matsuoka: *Eng. Fract. Mech.*, 2010, vol. 77, pp. 1926–40.
40. S.P. Lynch: in *Gaseous Hydrogen Embrittlement of Materials in Energy Technologies*, R.P. Gangloff and B.P. Somerday, eds., Woodhead Publishing Limited, Cambridge, U.K., 2012, vol. 1, pp. 274–378.
41. I.M. Robertson, M.L. Martin, and J.A. Fenske: in *Gaseous Hydrogen Embrittlement of Materials in Energy Technologies*, R.P. Gangloff and B.P. Somerday, eds., Woodhead Publishing Limited, Cambridge, U.K., 2012, vol. 2, pp. 166–206.
42. Y. Ro, S.R. Agnew, and R.P. Gangloff: *Metall. Mater. Trans. A*, 2007, vol. 38A, pp. 3042–62.
43. D.C. Slavik and R.P. Gangloff: *Acta Mater.*, 1996, vol. 44, pp. 3515–34.
44. V.K. Gupta and S.R. Agnew: *Int. J. Fatig.*, 2011, vol. 33, pp. 1159–74.
45. D.C. Slavik, C.P. Blankenship, E.A. Starke, and R.P. Gangloff: *Metall. Mater. Trans. A*, 1993, vol. 24A, pp. 1807–17.
46. Y. Ro, S.R. Agnew, and R.P. Gangloff: *Metall. Mater. Trans. A*, 2012, in press.
47. Y. Ro, S.R. Agnew, and R.P. Gangloff: in *Fourth International Conference on Very High Cycle Fatigue*, J.E. Allison, J.W. Jones, J.M. Larsen, and R.O. Ritchie eds., TMS-AIME, Warrendale, PA, 2007, pp. 407–20.
48. R.P. Wei, P.S. Pao, R.G. Hart, T.W. Weir, and G.W. Simmons: *Metall. Mater. Trans. A*, 1980, vol. 11A, pp. 151–58.
49. M. Gao, P.S. Pao, and R.P. Wei: *Metall. Mater. Trans. A*, 1988, vol. 19A, pp. 1739–50.
50. P.S. Pao, M. Gao, and R.P. Wei: in *Basic Questions in Fatigue*, R.P. Wei and R.P. Gangloff eds., ASTM STP 924, ASTM International, West Conshohocken, PA, 1988, pp. 182–95.
51. R.P. Wei and M. Gao: in *Hydrogen Effects on Material Behavior*, N.R. Moody and A.W. Thompson eds., TMS-AIME, Warrendale, PA, 1990, pp. 789–813.
52. J.T. Burns, J.M. Larsen, and R.P. Gangloff: *Fatig. Fract. Eng. M.*, 2011, vol. 34, pp. 745–73.
53. D.L. McDowell, K. Gall, M.F. Horstemeyer, and J. Fan: *Eng. Fract. Mech.*, 2003, vol. 70, pp. 49–80.
54. J.M. Papazian, E.L. Anagnostou, S.J. Engel, D. Hoitsma, J. Madsen, R.P. Silberstein, G. Welsh, and J.B. Whiteside: *Eng. Fract. Mech.*, 2009, vol. 76, pp. 620–32.
55. A. Shyam, J.E. Allison, C.J. Szczepanski, T.M. Pollock, and J.W. Jones: *Acta Mater.*, 2007, vol. 55, pp. 6606–16.
56. R. Jones, S. Pitt, and D. Peng: *Eng. Fail. Anal.*, 2008, vol. 15m, pp. 1130–11.
57. E.R. de los Rios and A. Navarro: *Philos. Mag. A*, 1990, vol. 61, pp. 435–49.
58. J.A. Harter: <http://www.stormingmedia.us/13/1340/A134073.html>, AFRL/VASM, Wright-Patterson AFB, OH, 2008.
59. J. Payne, G. Welsh, R.J. Christ Jr., J. Nardiello, and J.M. Papazian: *Int. J. Fatig.*, 2010, vol. 32, pp. 247–55.
60. ASTM G34-01, ASTM International, West Conshohocken, PA, 2007.
61. ASTM E466-07, ASTM International, West Conshohocken, PA, 2007.
62. ASTM E-1012-05, ASTM International, West Conshohocken, PA, 2005.
63. P.R. Wiederhold: *Water Vapor Measurement Methods and Instrumentation*, CRC Press, New York, NY, 1997.
64. ASTM E647-05, ASTM International, West Conshohocken, PA, 2006.
65. I.M. Chakravarti, R.G. Laha, and J. Roy: *Handbook of Methods of Applied Statistics*, Wiley, New York, 1967.
66. J.C. Newman and I.S. Raju: in *Computational Methods in the Mechanics of Fracture*, S.N. Atluri ed., Elsevier Science, New York, NY, 1986.
67. R.W. Bush and J.H. Ai: University of Virginia, Charlottesville, VA, unpublished research, 2010.

68. F.S. Lin and E.A. Starke: *Mater. Sci. Eng.*, 1979, vol. 39, pp. 27–41.
69. F.S. Lin and E.A. Starke: *Mater. Sci. Eng.*, 1980, vol. 43, pp. 65–76.
70. J. Ruiz and M. Elices: *Acta Mater.*, 1997, vol. 45, pp. 281–93.
71. I.S. Cole, P.A. Corrigan, G.C. Edwards, D. Followell, S. Galea, W. Ganther, B.R. Hinton, T. Ho, C.J. Lewis, T.H. Muster, D. Paterson, D.C. Price, D.A. Scott, and P. Trathen: in *Materials Forum*, S. Galea and A. Mita eds., Institute of Materials Engineering Australasia, North Melbourne, Australia, 2009, vol. 33, pp. 27–35.
72. I. Cole: DSTO, Melbourne, Australia, personal communication, 2011.
73. F.G. Nelson and J.G. Kaufman: *Fracture Toughness Testing at Cryogenic Temperatures*, ASTM STP 496, ASTM International, West Conshohocken, PA, 1971, pp. 27–39.
74. Air Force Ballistic Missile Division, AF-04(647)-593-3, National Bureau of Standards/Cryogenic Engineering Laboratory, Boulder, CO, 1959.
75. K.V. Jata and E.A. Starke: *Scripta Metall. Mater.*, 1988, vol. 22, pp. 1553–56.
76. T.L. Anderson: *Fracture Mechanics: Fundamentals and Applications*, CRC Press, Boca Raton, FL, 1991.
77. Z.M. Gacem and R.P. Gangloff: in *Chemistry and Electrochemistry of Corrosion and Stress Corrosion Cracking: A Symposium Honoring the Contributions of R.W. Staehle*, R.H. Jones ed., TMS-AIME, Warrendale, PA, 2001, pp. 501–21.
78. M. Wilhelm, M. Nageswararao, and R. Meyer: in *Fatigue Mechanisms*, J.T. Fong ed., ASTM STP 675, ASTM International, West Conshohocken, PA, 1979, pp. 214–33.
79. T.W. Weir, G.W. Simmons, R.G. Hart, and R.P. Wei: *Scripta Metall. Mater.*, 1980, vol. 14, pp. 357–64.
80. M. Watanabe: *J. Phys. Chem. Solids*, 2010, vol. 71, pp. 1251–58.
81. G.M. Scamans, R. Alani, and P.R. Swann: *Corros. Sci.*, 1976, vol. 16, pp. 443–59.
82. M. Francis: Ph.D. Dissertation, University of Virginia, Charlottesville, VA, 2012.
83. S.W. Smith and J.R. Scully: *Metall. Mater. Trans. A*, 2000, vol. 31A, pp. 179–93.
84. R.P. Wei: *Fatig. Fract. Eng. M*, 2002, vol. 25, pp. 845–54.
85. R. Braun, H.J. Schluter, and H. Zuchner: in *Hydrogen Transport and Cracking in Metals*, A. Turnbull ed., The Institute of Metals, Teddington, U.K., 1994, pp. 280–88.
86. J.R. Scully, G.A. Young, and S.W. Smith: *Mater. Sci. Forum*, 2000, vol. 331–333, pp. 1583–99.
87. J.R. Scully and G.A. Young: in *Gaseous Hydrogen Embrittlement of Metals in Energy Technologies*, R.P. Gangloff, B.P. Somerday eds., Woodhead Publishing Ltd., Cambridge, U.K., 2012, vol. 1, pp. 707–59.
88. G.A. Young and J.R. Scully: *Acta Mater.*, 1998, vol. 46, pp. 6337–49.
89. A.S. El-Amoush: *J. Alloys Compd.*, 2008, vol. 465, pp. 497–501.
90. N. Takano: *Mater. Sci. Eng. A*, 2008, vol. 483–484, pp. 336–39.
91. J.T. Burns: Ph.D. Dissertation, University of Virginia, Charlottesville, VA, 2010.
92. H.K. Birnbaum, C. Buckley, F. Zeides, E. Sirois, P. Rozenak, S. Spooner, and J.S. Lin: *J. Alloys Compd.*, 1997, vol. 253, pp. 260–64.
93. K.R. Hebert, T. Gessmann, K.G. Lynn, and P. Asoka-Kumar: *J. Electrochem. Soc.*, 2004, vol. 151, pp. B22–26.
94. O.D. Smiyan, M.V. Coval, R.K. Melekov, N.L. Korobanova, A.M. Krutsan, and V.A. Yakovchik: *Soviet. Mater. Sci.*, 1983, vol. 19, pp. 422–26.
95. A.T. Kermanidis, P.V. Petroyiannis, and S.G. Pantelakis: *Theory Appl. Fract. Mech.*, 2005, vol. 43, pp. 121–32.
96. P.V. Petroyiannis, A.T. Kermanidis, P. Papanikos, and S.G. Pantelakis: *Theory Appl. Fract. Mech.*, 2004, vol. 41, pp. 173–83.
97. C. Atkinson: *J. Appl. Phys.*, 1971, vol. 42, pp. 1994–97.
98. S. Adhikari, J.H. Ai, K.R. Hebert, K.M. Ho, and C.Z. Wang: *Electrochim. Acta*, 2010, vol. 55, pp. 5326–31.
99. C.E. Buckley and H.K. Birnbaum: *J. Alloys Compd.*, 2002, vol. 330, pp. 649–53.
100. D.M. Li, R.P. Gangloff, and J.R. Scully: *Metall. Mater. Trans. A*, 2004, vol. 35A, pp. 849–64.
101. C. Wolverton, V. Ozolins, and M. Asta: *Phys. Rev. B*, 2004, 69(144109), pp. 1–16.
102. G. Lu and E. Kaxiras: *Phys. Rev. Lett.*, 2005, vol. 94 (155501), pp. 1–4.
103. M.O. Speidel: *Hydrogen Embrittlement and Stress Corrosion Cracking*, G. Gibala, R.F. Hehemann, eds., ASM International, Materials Park, OH, 1984, pp. 271–96.
104. R.W. Siegel: *J. Nucl. Mater.*, 1978, vol. 69–67, pp. 117–46.
105. A.M. Lucente and J.R. Scully: *Corros. Sci.*, 2007, vol. 49, pp. 2351–61.
106. J.H. Ai: University of Virginia, Charlottesville, VA, unpublished research, 2010.
107. G.M. Pressouyre: *Acta Metall.*, 1980, vol. 28, pp. 895–11.
108. J. Toribio and V. Kharin: *J. Mater. Sci.*, 2006, vol. 41, pp. 6015–25.
109. J. Toribio and V. Kharin: *Fatig. Fract. Eng. M*, 1997, vol. 20, pp. 729–45.
110. D.C. Ahn, P. Sofronis, and R. Minich: *J. Mech. Phys. Solids*, 2006, vol. 54, pp. 735–55.
111. A. Pedersen and H. Jonsson: *Acta Mater.*, 2009, vol. 57, pp. 4036–45.
112. J.P. Hirth: *Metall. Mater. Trans. A*, 1980, vol. 11A, pp. 861–90.
113. T.Y. Zhang, H. Shen, and J.E. Hack: *Scripta Metall. Mater.*, 1992, vol. 27, pp. 1605–10.
114. R. Bullough and R.C. Newman: *Rep. Prog. Phys.*, 1970, vol. 33, pp. 101–48.
115. E. Clouet: *Acta Mater.*, 2006, vol. 54, pp. 3543–52.
116. C. Gasqueres, C. Sarrazin-Baudoux, J. Petit, and D. Dumont: *Scripta Mater.*, 2005, vol. 53, pp. 1333–37.
117. S. Richard, C. Gasqueres, C. Sarrazin-Baudoux, and J. Petit: *Eng. Fract. Mech.*, 2010, vol. 77, pp. 1941–52.
118. J.C. Newman: *Behavior of Short Cracks in Airframe Components - AGARD SP-328*, AGARD, H. Zocher, eds., Toronto, CA, 1982, pp. 6.1–6.26.
119. J.C. Newman, X.R. Wu, M.H. Swain, W. Zhao, E.P. Phillips, and C.F. Ding: *Fatig. Fract. Eng. M*, 2005, vol. 23, pp. 59–72.
120. X.R. Wu, J.C. Newman, W. Zhao, M.H. Swain, C.F. Ding, and E.P. Phillips: *Fatig. Fract. Eng. M*, 1998, vol. 21, pp. 1289–06.
121. K. Shiozawa, Y. Tohda, and S.M. Sun: *Fatig. Fract. Eng. M*, 1997, vol. 20, pp. 237–47.
122. B.A. Bilby, A.H. Cottrell, and K.H. Swindon: *Proc. R. Soc. Lond. A*, 1966, vol. 272, pp. 304–14.